Thesis Report

Aerosol Optical Depth and Cloud Parameters from Ascension Island retrieved with a UV-depolarisation Lidar

An outlook on the validation

Manon Schenkels
28th March 2018

Koninklijk Nederlands
Meteorologisch Instituut
Ministerie van Infrastructuur en Milieu

Utrecht University

Aerosol Optical Depth and Cloud Parameters from Ascension Island retrieved with a UV-depolarisation Lidar

An outlook on the validation

Manon Schenkels
Student number: 6036996

Supervisors:
Martin de Graaf
Rupert Holzinger

A thesis submitted in partial fulfillment of the degree of Master of Science
at Utrecht University, Institute for Marine and Atmospheric Research, The Netherlands.

28th March 2018, Utrecht, The Netherlands

Abstract

Aerosol-Cloud Interactions (ACIs) are one of the least understood climate feedbacks. Ground-based remote sensing has a large potential to study these interactions. In this study a UV-depolarisation lidar has been set up on Ascension Island, a remote island in the southeast Atlantic Ocean, for one month in summer 2016 and one month in summer 2017, to study the aerosol, cloud microphysical properties, and their interaction. In clear-sky (cloud-free) periods, the backscattered signal is used to calculate the Aerosol Optical Depth (AOD). The AOD is a measure of the attenuation of the lidar beam due to suspended particles, which can be estimated in clear-sky, by integration of the extinction profile over the column and accounting for the Rayleigh (molecular) attenuation. A UV-depolarisation lidar measures not only the backscattered signal but also the depolarisation of the returned signal. Depolarisation of the lidar beam can occur due to multiple-scattering inside liquid water clouds. The multiple-scattering inside the cloud near the cloud-base was simulated using a Monte Carlo (MC) model inside an idealised semi-adiabatic liquid water cloud. Using lookup tables generated by the MC model, the cloud microphysical properties such as the cloud droplet number concentration and the effective radius were derived from the depolarisation ratio observed by the lidar. The aim of the study was to validate these retrieval methods. The AOD product was compared to AERONET data and data from hand-held sun-photometers. The multiple-scattering (MS) based inversion method for the retrieval of the cloud droplet effective radius was compared to a method using radar observations on the island from the US ARM mobile facility.

The lidar AOD retrievals show similar values in 2016 as the AERONET data. In 2017 the AOD lidar retrievals do not correlate well with the AERONET, Calitoo and Microtops data. Misalignment has caused difficulties in the AOD retrieval in 2017. The effective radius in clouds retrieved from the lidar data could not be compared to the methods with radar data in 2016, because the radar was operating for only 9 days of our measurement period. In 2017 the lidar retrieved effective radius agrees within the error bands with the radar retrieved effective radius. These results show the UV-depolarisation lidar to be a potentially useful instrument to study the AOD and the cloud droplet effective radius. With more research focusing on the validation of the methods to employ the lidar, the instrument could prove valuable for Aerosol-Cloud Interaction monitoring.

Keywords: UV-depolarisation lidar, aerosol optical depth, multiple-scattering, cloud effective radius, AERONET, Calitoo, Microtop, Cloud radar, Ascension Island

Acknowledgements

Foremost, I would like to express my gratitude to my supervisors Rupert Holzinger and Martin de Graaf for the support and feedback that they provided on my thesis. Next to my advisers I also wish to thank Dave Donovan for the support and advice regarding the UV-depolarisation lidar and the MS based inversion method. Thanks also to Thomas Röckmann for taking part in my thesis examination.

Thanks to CLARIFY, and the campaign PI Jim Haywood who made it possible to operate the lidar on Ascension Island, for their warm and generous hospitality during the campaign and the sharing of their Microtop data gathered during the campaign. Thanks to Susannah Rastall for the organisation of the lidar transport. Thanks to Joss Kent and Dave Tiddeman for the chats about the Leosphere Lidar and the insight in the lidar set-up in the CLARIFY aircraft. Thanks to the US ARM Ascension Island mobile facility, its lead scientist Paquita Zuidema and the technical staff on the island, Wagner and Bruno. Radiosondes, Cloud Radar, Ceilometer and Microwave Radiometer Data were obtained from the Atmospheric Radiation Measurement (ARM) Program sponsored by the U.S. Department of Energy, Office of Science, Office of Biological and Environmental Research, Climate and Environmental Sciences Division. Thanks to AERONET for their level 2.0 Aerosol Optical Depth (AOD) data. And I gratefully acknowledge the NOAA Air Resources Laboratory (ARL) for the provision of the HYSPLIT transport and dispersion model used in this report.

I also thank Jessica Brown and Elma Tenner for their previous work on the UV-depolarisation lidar for their thesis at the KNMI (Brown, 2016; Tenner, 2017). I thank Bram for his support throughout the whole process. Also thanks to my brother Tom for the discussions and objective view on my research, and the use of his thesis as an example for the structure in my thesis.

Contents

List of Figures

List of Tables

1. Introduction

Aerosol-Cloud Interactions (ACIs) are one of the least understood climate feedbacks, according to the Fifth Assessment Report of the Intergovernmental Panel on Climate Change (*IPCC, 2014*). To gain more insight on these effects different types of research are done. On the global scale, the aerosol effects on clouds are studied using satellite remote sensing observations and by model studies, at smaller scales studies are carried out using surface remote sensing or a combination of aircraft in-situ data with surface remote sensing.

Aerosols can have various effects on clouds, which are explained extensively in Lohmann and Feichter, 2005. In this research we focus on the first indirect effect, the Twomey effect, (Twomey, 1977). The Twomey effect is related to the number of available Cloud Condensation Nuclei (CCN), which is a subset of the aerosols present. In low-level liquid stratocumulus clouds with a constant Liquid Water Content (LWC), the cloud droplet number concentration (N_d) increases and the size of the cloud droplets decreases with an increase of CCN. The increase of N_d and decrease of the size of the cloud droplets increases the optical thickness and cloud reflectivity. This is a secondary effect and is called the cloud albedo effect, directly resulting from the Twomey effect (Allison McComiskey et al., 2009). Another result of the Twomey effect is the delay of precipitation (Lohmann and Feichter, 2005).

Ascension Island is chosen as study area for its generally well defined stratocumulus deck (Norris, 1998), its remote location and its high level of biomass burning aerosols (Swap et al., 1996), released from the African continent from July through October, because of the dry season. This makes the island a perfect location for studying the ACIs. Ascension Island is midway the Atlantic Ocean between Africa and America, just south of the equator, in a sub-tropical region. The aerosols that are mostly observed at Ascension Island are dust particles from the Sahara or smoke particles from biomass burning events south of the Sahara, besides marine aerosols (Swap et al., 1996). The aerosol distribution across the ocean depends on the wind speed and direction.

A UV-depolarisation lidar (LIght Detection And Ranging) is a remote sensing laser instrument, which makes height resolved measurements of the aerosol and cloud backscatter. The lidar is a promising instrument to examine the vertical profiles for clouds, aerosols and the ACI (Mamouri and Ansmann, 2016). Often used parameters to represent ACI are the Aerosol Optical Depth (AOD) and Aerosol Index (AI) for the aerosols[1]. And the effective radius (R_{eff}), cloud droplet num-

[1]The AOD is the integrated aerosol extinction profile. The AI is a measure of how much the wavelength dependence of the total backscatter (molecular and aerosol scattering and absorption) differs from the wavelength dependence of the pure molecular backscatter (Rayleigh scattering, by the molecules in the air only).

ber concentration (N_d), liquid water path (LWP) and cloud optical depth for the clouds[2]. The vertical extinction profile can be integrated over the whole column on cloud-free periods to get the AOD, following the Klett inversion (Klett, 1981). The cloud parameters are retrieved in this study from the lidar with a method developed by Donovan et al. (D. P. Donovan et al., 2015). The Multiple Scattering (MS) based inversion method uses the polarisation of the lidar pulses due to multiple scattering in liquid water clouds.

Several studies have been performed in the past years, using ground-based remote sensing instruments, studying the range of interactions that take place between aerosols and clouds. Although the methods are similar the measured parameters differ a lot. Generally, A. McComiskey and Feingold (2012) conclude that regarding the differences in temporal and spatial scale, "the numerous process studies that have attempted to assess the magnitude of these effects have generated conflicting answers, and even the sign of the cloud water response to changes in the aerosol is in question".

AOD measurements are widely done with lidars, the retrieval of microphysical cloud properties not so much. The depolarisation lidar is an instrument with high potential for the retrieval of cloud microphysical properties due to the simulation of multiple scattering in the clouds and the depolarisation ratio. To check how the depolarisation lidar is doing for the retrieval of the AOD and the cloud parameters and to study the ACIs compared to other methods, in this thesis various methods are compared, by checking whether the retrieved parameters agree within their error bands.

The AOD data used for the intercomparison is from AERONET, Calitoo measurements and Microtops measurements. The Calitoo Aerosol photometer and Microtops were used to measure AODs at clear-sky moments manually, the AErosol ROotic NETwork (*AERONET*) which has a station at Ascension Island with an automated sunphotometer.

The R_{eff} for intercomparison is retrieved with methods described by (Frisch, Fairall et al., 1995) from radar reflectivity measurements gathered with cloud radars. These cloud radars are operated by the Atmospheric Radiation Measurement Climate Research Facility (*ARM*) as part of a temporal site as Ascension Island. This ARM site is the implementation of the Layered Atlantic Smoke Interactions with Clouds (*LASIC*) campaign.

Our research was part of the UK measurement campaign CLouds and Aerosol Radiative Impacts and Forcing (*CLARIFY*). CLARIFY flew with Ascension as base with an aircraft full of atmospheric in situ and remote sensing instruments. The in-situ measurements from CLARIFY provide an excellent opportunity to verify the retrieval method for the cloud parameters and the AOD retrieval. Although care

[2]The effective radius of cloud droplets is the area weighted mean radius of the cloud droplets, $R_{eff} = \frac{\int_0^\infty R^3 n(R) dR}{\int_0^\infty R^2 n(R) dR}$, where $n(R)$ is the cloud droplet particle size distribution. N_d is in cm^{-3} and the LWP is the integrated liquid water content in a column in $\mathrm{g\,m}^{-3}$.

should be taken for the spatial, horizontal and vertical difference and for the fact that we only retrieve the cloud parameters for the cloud base.

Methods to evaluate the aerosol and cloud vertical profiles with a ground-based depolarisation lidar is valuable for ACI and global warming related research. Therefore, we focus on the evaluation of these methods for acquiring such data.

The objectives of this research are:

RQ1: How do the lidar products compare to other methods?: **1a)** How does the AOD retrieved from the lidar compare to the AOD gathered from AERONET, the Calitoo and Microtops? **and 1b)** How does the R_{eff} retrieved from the lidar compare to the R_{eff} retrieved from the radar data with Frischs methods?

RQ2: How do the two years of lidar measurements compare in terms of the AOD and R_{eff}?

RQ3: Is the accuracy of the retrievals from the lidar sufficient to say something about the ACI above Ascension Island?

2. Field Campaign

2.1. Study area

Ascension Island(7.9^o S, 14.4^o W) is an isolated volcanic island surrounded by the South Atlantic Ocean, with an area of approximately 88 km^2. The island has a hot desert climate. The annual rainfall is low, although it is in the tropical zone (Dorman and Bourke, 1981) with an average value of 142 mm/yr at Ascension Island.

Figure 2.1: Map showing the location of the study area, Ascension Island.

The prevailing wind in the boundary layer on the island is from the (east-) southeast, because of the dominating subtropical trade wind (Kim et al., 2003). These trade winds are almost invariant. This means, as can be seen in figure 2.3, that the wind flows over the highest point of the island first. Above the boundary layer (1200 - 2000 m above sea level, depending on the diurnal cycle) the wind is coming from the equatorial regions. These air masses have dominantly been last in contact with the ground in tropical Africa (Greatwood et al., 2017). Swap et al., 1996 found that air parcels take around 7 days to travel from Namibia to Ascension Island between 900 hPa and 800 hPa when stability is sustained. With back trajectories the movement of air parcels is recalculated and the aerosols above Ascension Island can be tracked back to their source.

2.2. Campaigns

In 2016 the lidar was operated at Ascension Island by KNMI. In 2017, the research corroborated the UK measurement campaign CLoud-Aerosol-Radiation Interactions and Forcing (*CLARIFY*). During CLARIFY an aircraft was operated with As-

cension as base, full of atmospheric measurement instruments, in situ and remote sensing. Airborne aerosol and cloud observations were in 2017 also performed during a NASA campaign, ObseRvations of Aerosols above CLouds and their intEractionS (*ORACLES*), having Sao Tome as a base. Their aircraft flew predominantly north-east of Ascension Island. With Namibia as base, a french campaign, AErosol RadiatiOn and CLOuds in Southern Africa (*AEROCLO-SA*), flew with the same incentive during the 2017 period. A large area of the South-East Atlantic was covered with in-situ measurements during our 2017 measurement period, shown in figure 2.2. All studying the effect of aerosols on clouds, radiation and the climate.

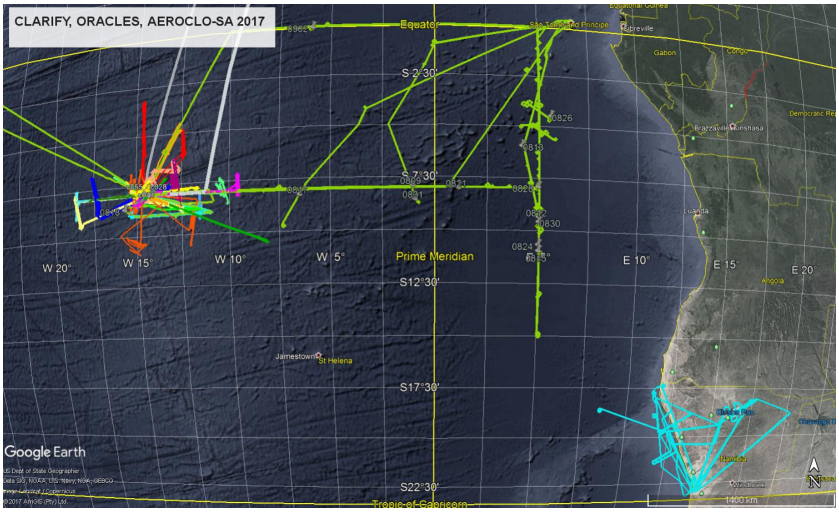

Figure 2.2: Map showing the locations of the Aircraft Campaings in 2017, CLARIFY on the left in rainbow colors, with Ascension as base. ORACLES in the north, shown with the green lines, with Sao Tome as their base and AEROCLO-SA from Africa, shown with the blue lines, with Namibia as their base.

2.3. Instrumentation

For this study, data was collected with a ground-based UV-depolarisation lidar. The lidar was set-up in both years on the airport site, shown in figure 2.3. For both measurement periods, the lidar was set up for a total duration of 26 days. In 2016 the lidar was non-operational due to power cuts and to computer malfunction from the morning of the 24th of August until the evening of the 27th of August. In 2017 more computer malfunctioning appeared but for shorter duration, so no full days, but only parts of days are missing in the data.

Radiosonde data, gathered by ARM, was used to calibrate the lidar for the Rayleigh scattering. The radiosondes, released from the airport site, gather in situ data for the vertical profiles of temperature, pressure and relative humidity. They were launched 8 times a day in 2016 and 4 times a day in 2017. The radiosonde

data was interpolated to the time and height resolution of the lidar. From this data the molecular extinction and backscatter coefficients were calculated.

A Calitoo Aerosol photometer was used occasionally in 2017, when there was clear sky, to measure the AOD. These measurements were performed from the airport site or from Georgetown, 5 km north from the airport site. AERONET has a site at Ascension Island, from which we can use the AOD data. In 2017 the AOD was also measured by the CLARIFY team, with Microtops, comparable aerosol photometers as the Calitoo, although not in accuracy. These products offer the AOD products, with which we can validate our AOD retrievals. For the cloud product comparison, data from the ARM site is used for both measurement periods. The products we have used were measured with a Ceilometer, Cloud Radars and a Microwave Radiometer (MWR), all located at the main ARM site, situated 6 km east from the airport site, at around 365 m above mean sea level. This location is also shown in the map below.

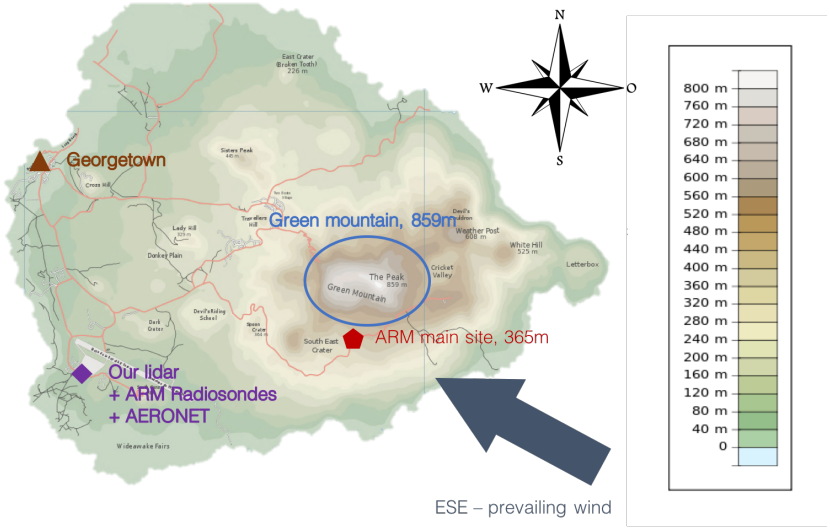

Figure 2.3: Ascension Island layout of instrumentation.

As observational data, two periods of measurements were used, one month from summer 2016 and one month from summer 2017. In these periods other atmospheric observations were done at or around Ascension Island which offer data to compare the processed lidar data with. In the table below an overview of general information and some meteorological parameters is shown for both of our measurement periods.

Table 2.1: Table with general information for the two periods of measurements with the UV-depolarisation lidar.

Dates	**3 sept 2016 - 29 sept 2016**	**15 aug 2017 - 10 sept 2017**
Location	Airport site	Airport site
Full days	21	16
Measured in total	537 hours	568 hours
Other campaigns	ARM, ORACLES	ARM, CLARIFY, ORACLES, AEROCLOSA
Average Surface temperature	21.19 ^{o}C	22.78 ^{o}C
Average Atmospheric pressure	97.78 kPa	97.71 kPa
Average Relative humidity	90.39 %	82.31 %
Average Wind direction	East-Southeast	East-Southeast
Average Wind speed	7.72 m/s	7.12 m/s

2.3.1. UV-depolarisation lidar

A LIDAR (LIght Detection And Ranging) is a remote sensing laser instrument. It has a laser on the transmission side and photomultipliers to detect the incoming radiation on the receiver side. The linearly polarized light transmitted by the laser travels through the air until it is absorbed or scattered by a molecule, aerosol or cloud droplet. When the light is only scattered once and returns in the direction of the lidar, is it termed single-scattering. When single-scattering occurs with a spherical particle, like a liquid water cloud droplet, the light will return with the same polarisation as it is transmitted by the laser, the light is parallelly polarized. The light can become depolarised, when it is scattered by a non-spherical particle, mostly ice or aerosol particles, or because of multiple scattering. Multiple scattering occurs when the light is scattered more than once by a particle. This multiple scattering is accounted for with an inversion method in the MS based inversion method.

Before the light is actually measured it goes through a filter, which will filter out the diffuse sunlight, through a lens, to focus the light. And in the end the return signal is split using a polarized beam-splitter into components whose plane of polarization is parallel and perpendicular to the transmidded light polaization plane. After the incoming light is split, it is detected by the photo-multiplier tubes (PMTs).

At the receiver side of the lidar a certain percentage of incoming radiation is lost during the detection, because of the filtering, the lenses and the splitting. These factors are combined in the lidar calibration constant, C_{lid}. The values used for the lidar calibration constants are shown in table 2.2. This lidar constant differs for the

two separate channels as it depends on the seperate PMTs. Cross-talk between the channels can exist, due to the uncertainty of the beam-splitter and thus the presence of signal with orthogonal polarisation in each channel. This effect is a source of uncertainty in the estimation of the depolarisation ratio. A polarisation cross-talk parameter δ^{C} is defined to correct for this effect. To calibrate the parallel and perpendicular channels in relative sense, an inter-channel depolarisation calibration constant, C_r, is defined, the value for this calibration coefficient is assumed a priori. To make sure that the inversion algorithm does not depend on the absolute calibration of the lidar, which is often not good, the attenuated backscatter normalised by the maximum value of the parallel attenuated backscatter is used.

Figure 2.4: Leosphere ALS-450 UV-depolarisation lidar setup during the field campaign. (7.97° S, 14.35° W)

Figure 2.5: Calitoo Aerosol photometer used during the field campaign.

Table 2.2: Lidar calibration constants for the inversion process.

Constant	Value in 2016	Value in 2017
C_{lid}	9.5 ± 1.0	9.5 ± 1.0
δ^{C}	0.97	0.87
C_r	1/0.026	1/0.031
FOV interpolation factor	0.14	0.14

The lidar that was used is a commercial Leosphere ALS-450 operating at 355 nm, pointed vertically with a zenith angle of 3 degree (Leosphere, n.d.). It has a tripled Nd-Yag laser with an energy of 16 mJ per pulse. The pulse duration is 5 ns and it fires with a frequency of 20 Hz. The lidar has a vertical resolution of 15 m and a 30 second time interval. So 600 pulses are averaged, to get the 30 second time interval. The lidar was positioned 76 m above mean sea level. The laser beam and receiver Field-Of-View (FOV) have an incomplete overlap in the lowest 200 m above the lidar, the system measures the backscatter from 200 m above the lidar. In 2016 the data had a good signal-to-noise ratio up to 20 km, in 2017 this was only up to 15 km, because of a misalignment.

2.3.2. Calitoo Aerosol photometer

The Calitoo is a hand-held sun photometer (Tenum, n.d.). It needs to be directed to the sun manually. It measures the incoming radiation flux, which is a function of radiation emitted by the sun and the effect of the atmosphere. From this incoming radiation flux, the total extinction is derived. The effect of the atmosphere is the atmospheric absorption and scattering from the molecules in the air, calculated from the measured pressure and temperature, and the extinction by the ozone column. Climatology data is used for the ozone column, to subtract from the total extinction in the profile. After correcting the total extinction for this molecular and ozone absorption and scattering, the AOD is calculated from the aerosol extinction (absorption and scattering) integrated over the column. The AOD is calculated for three different wavelengths in the visible light spectrum: blue (465nm), green (540nm) and red (615nm). The calculation of the AOD is done using the raw brightness measurements, the calibration coefficients, the atmospheric pressure, date and the GPS position.

The total AOD at wavelenght λ is derived following Beer-Lambert-Bouguer's law: $V_\lambda = V_{0\lambda} D^{-2} \exp(-\tau_\lambda M)$, where V_λ is the signal measured by the instrument at wavelength λ, $V_{0\lambda}$ is the extraterrestrial signal at wavelength λ, D is the earth-sun distance in astronomical units at time of observation, τ_λ is the total optical thickness at wavelength λ, consisting of the molecular, aerosol and ozone optical thickness and M is the optical air mass (Ichoku et al., 2002). Beer's law is only accurate when multiple-scattering is not important, when there are no clouds.

The Calitoo was operated from the airport site or from Georgetown, 5 km north from the airport site, see figure 2.3. In total 15 values for the AOD were measured during the period in 2017. The AOD measured for the blue wavelength is used for the intercomparison as it is the closest to the wavelength of the lidar. The uncertainty in the value for the AOD measured with the Calitoo is dominated by the variation of the averaged measurements, gathered within 5 minutes.

2.3.3. AERONET

AERONET offers their AOD data processed on the website for various wavelengths, the AOD measered at a wavelength of 340 nm is used for the intercomparison. AERONET is a network of several ground-based sun-photometers distributed globally gathering direct sun measurements, to calculate the wavelength dependent AOD (Holben et al., 1998). The instruments are automatic tracking sun and sky scanning radiometers with a 1.2^{o} field of view. They measure the direct sun measurements every 15 minutes at 8 wavelengths. An ion-assisted deposition interference filter with a band pass of 2 nm is positioned in front of the detector for the 340 nm measurement. The AERONET data we used in this study was quality- and cloud-screened. The AERONET AOD data measured at the wavelength of 340 nm has an uncertainty of 0.021. This is due to atmospheric pressure variation when assuming there is a 3 % maximum departure from mean surface pressure (Eck et al., 1999).

2.3.4. Microtops

Microtops are also hand-held sun photometers. They work similar as the Calitoo. With a moving filter wheel, the filters are changed inside the instrument, to measure the direct sunlight at five different wavelengths. The filters used in the channels have a band pass of 10 nm for all channels. The AOD gathered with the Microtops is calculated with the same equation as was stated for the Calitoo.

The data from the Microtops was shared by the CLARIFY team on Ascension Island. They operated two instruments every time at the same moment. The average of the AOD is calculated for the wavelength of 550 nm from the two instruments. The instrument uncertainty of the Microtop is comparable to the uncertainty from AERONET (Ichoku et al., 2002). At 550 nm, the uncertainty in the Microtops AOD measurements is 0.03. We also calculate the variation in the measurements gathered by the two instruments within 5 minutes.

2.3.5. ARM instruments for Cloud Parameter retrievals

The cloud parameters used for the intercomparison are calculated with the use of reflectivity data gathered by the Cloud Radars from ARM and the LWP data measured by the Microwave Radiometer. Because there is no Cloud Radar at the air-

port site, for both products the data from the main ARM site were used. In 2016 the W-band Scanning ARM Cloud Radar (WSACR) (*(ARM), Instruments: WSACR* n.d.) was operating from the start of our measurement period up until the 11th of september. In 2017 the Ka-band Scanning ARM Cloud Radar (KASACR) (*(ARM), Instruments: KASACR* n.d.) has been operating for the full period. The radars operate with a field of view of 0.3 degrees for both radars and a frequency of 94 GHz and 35.3 GHz respectively for the WSACR and KASACR. Vertical pointing scans are taken each hour, for a duration of 4 minutes. The products with a time-resolution of 2 seconds and a vertical resolution of 30 m, are available online. For the LWP, Microwave Radiometer (MWR) (*(ARM), Instruments: MWR* n.d.) data were used, which was available online for the period in 2016, but not yet for the period in 2017. The LWP is measured and processed once every 30 seconds.

Cloud Radars

A Cloud Radar is like a lidar an active remote sensing instrument but transmits pulses in the radio-frequency instead of in the visible light or ultraviolet. Both the radars include a Ka-band radar (2 kW peak power), the WSACR also has a second radar, the W-band (1.7 kW peak power) (*(ARM), Instruments: WSACR* n.d.). The ARM cloud radars are special because of their scanning strategies. For this research the vertical-pointing mode is used, in which the radar is not scanning. From the vertical pointing scans with the cloud radar, the 2D radar reflectivity factor, Z, is used. This reflectivity is the backscattered radio frequency from cloud droplets or precipitation. The radar has a transmitter in the center, the receiver is in a circle around this trasmittor. The radiation trasmitted by the radar travels through the air until it is reflected back by a cloud droplet or precipitation. The product we collected from the ARM database is a height-time product of the reflectivity in the vertical above the radar.

Microwave Radiometer

A microwave radiometer (MWR) is a radiometer measuring energy emitted by gas or particles in the atmosphere in the microwave (millimetre-to-centimetre wavelengths) range. The ARM MWR is a sensitive microwave receiver that detects the microwave emissions of the water vapor and liquid water molecules in the atmosphere at two frequencies: 23.8 and 31.4 GHz. (*(ARM), Instruments: MWR* n.d.). Water vapor has its absorption line around 23 GHz, liquid water emission increases with frequency, so the 31.4 GHz frequency is more sensitive to liquid water emission by hydrometeors. As the size of the hydrometeors increases, the frequency at which they emit energy is increasing. For example, large rain drops and larger frozen hydrometeors, having sizes of a few milimeters, emit energy at a frequency especially higher than 90 GHz so will not be detected by the MWR we used. Using a statistical retrieval

algorithm, the integrated water vapor and liquid water path are derived from the radiance measurements ((*ARM), Instruments: MWR* n.d.).

2.3.6. Overview of the instruments and products

An overview of all the products used in this study is given in the table below.

Table 2.3: Cloud and aerosol properties measured or derived, and used in this study, from the observations at Ascension Island.

Measured quantity	**Definition**	**Instrument(s)**
Attenuated backscatter coefficient	ATB ($\mathrm{m}^{-1}\,\mathrm{sr}^{-1}$)	Leosphere ALS-450
Pressure and Temperature profiles	P (Pa), T (K)	Radiosondes
Aerosol Optical Depth (AOD)	τ	Leosphere ALS-450
Cloud droplet effective radius	R_{eff} (µm)	Leosphere ALS-450
Aerosol Optical Depth (AOD)	τ	AERONET, Calitoo photometer, Microtops
Radar reflectivity factor	Z (dBZ or $\mathrm{m}^6\,\mathrm{m}^{-3}$)	WSACR/KASACR
Cloud liquid water path	LWP ($\mathrm{g}\,\mathrm{m}^{-2}$)	MWR
Cloud droplet effective radius	R_{eff} (µm)	WSACR/KASACR + MWR

3. Methods

Lidar data was processed to retrieve the AOD product and the R_{eff} as the cloud parameter used for the intercomparison. AERONET, Calitoo and Microtops measured AOD data was used to compare the lidar retrieved AODs. The AOD measurements from AERONET and the hand-held Calitoo and Microtops were performed on randomly distributed moments during the periods, because of the requirement of clear sky and direct sunlight. For the lidar measurements, the direct sunlight will cause solar background noise during the day, so the aerosol signals were generally more accurate during the night. In this study, selections in day and night time are used for the AOD retrieval. The R_{eff} is retrieved from the lidar using the MS based inversion method, and compared to R_{eff} calculated with Frischs methods using reflectivity data gathered with the Cloud Radars and LWP data gathered with the MWR. For the retrieval of the cloud parameter, low level marine stratocumulus clouds were selected. The cloud parameter results were only analyzed statistically, because the clouds could not be selected case-by-case because of the 6 km distance between the airport site from where we retrieved our product and the ARM site.

3.1. Lidar data processing

The lidar signal is detected as described in the previous chapter. The time after which photons are detected is translated to range, $z = \frac{ct}{2}$, where c is the speed of light and t the time after which the photon is detected. The detected signal over a vertical range can be analyzed with the three-component lidar equation (Measures, 1984, p. 237–243):

$$P(z) = \frac{C_{lid}}{z^2}(\beta_m(z) + \beta_a(z) + \beta_c(z))e^{-2\int_0^z(\alpha_m(z')+\alpha_a(z')+\alpha_c(z'))dz'} \tag{3.1}$$

where $P(z)$ is the received power as a function of range, C_{lid} is the lidar calibration constant, as described in section 2.3.1, z is the range, β is the backscatter coefficient divided into a molecular, aerosol and cloud component, denoted with subscripts m, a, c respectively. α is the extinction coefficient, also divided into the three components. The attenuated backscatter (ATB) is an atmospheric parameter, independent of instrumental effects, $ATB(z) = \frac{P(z)z^2}{C_{lid}}$, and $\beta(z) = \frac{\alpha(z)}{S(z)}$, where $S(z)$ is the extinction-to-backscatter ratio, or the lidar ratio. This ratio depends on the type of particle, composition, size or structure.

To examine the AOD, lidar measurements without cloud and precipitation, and without full irradiance by the sun should be considered. For the cloud parameter retrieval, low level homogeneous stratocumulus clouds are selected by eye. An example for both of the selections is shown in figure 3.1.

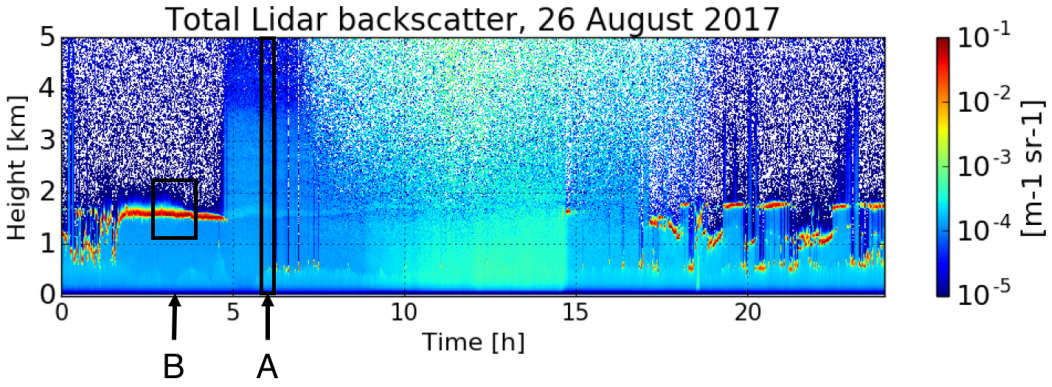

Figure 3.1: The total ATB in the lower troposphere (0-5 km), for the 26th of August 2017. Visualisation of the selections for the analysis of the aerosol profile, A, and a cloud, B.

There are six atmospheric unknowns in equation (3.1), the extinction coefficient α for the molecular, aerosol and cloud component, and the backscatter coefficient β for the molecular, aerosol and cloud component. These coefficients are discussed in the following paragraphs. First α_m and β_m, the molecular extinction and backscatter coefficients from Rayleigh scattering. Followed by the aerosol extinction and backscatter coefficients, α_a and β_a in the AOD retrieval section. The cloud extinction coefficient α_c is retrieved in the MS based inversion method. For the cloud parameter intercomparison R_{eff} is the parameter used, instead of α_c. The R_{eff} is directly dependent on α_c and the LWC.

3.1.1. Rayleigh scattering

The wavelength of the transmitted light λ, is 355 nm. Rayleigh scattering is strongly wavelength dependent, the particles diameter is only a fraction of the wavelength. At 355 nm, Rayleigh scattering, from the molecules in the air, is of big importance. The known molecular scattering is used to calibrate the lidar. With the data from radiosondes, the molecular particle density of the atmosphere, ρ_{atm}, is calculated with $\rho_{\text{atm}} = \frac{P}{T \times \rho_{\text{air}}}$ $\text{kg}\,\text{m}^{-3}$ where P is the measured pressure in Pa, T the measured temperature in K and ρ_{air} is the gas density of dry air, 287 $\text{J}\,\text{kg}^{-1}\,\text{K}^{-1}$. By multiplying the molecular Rayleigh backscattering cross section, $\sigma^R(\lambda) = 5.45 \left[\frac{550}{\lambda(\text{nm})}\right]^4 \times 10^{-32}$ $\text{m}^2\,\text{sr}^{-1}$, (Measures, 1984, p. 42) with the molecular particle density divided by the molecular mass, the molecular backscattering coefficient, β_m, is calculated, $\beta_m = \frac{\rho_{\text{atm}}}{\text{M}} \times \sigma^R$ $\text{m}^{-1}\,\text{sr}^{-1}$. With the Rayleigh extinction-to-backscatter ratio of $\frac{8\pi}{3}$sr (Guzzi, 2008, p. 231), the molecular extinction coefficient α_m can be calculated.

3.1.2. AOD retrieval

After selecting correct profiles to retrieve the AOD, a time average atmospheric extinction profile, α_{atm}, is retrieved with the lidar and then inverted to an aerosol extinction profile and AOD following the Klett inversion (Klett, 1981), a boundary-value problem, as described below. When there is no cloud, the lidar equation, (3.1), is only dependent on the aerosol and molecular components. We can define the total, atmospheric extinction coefficient as $\alpha_{atm}(z) = \alpha_a(z) + \alpha_m(z)$

A normalisation height was set where the aerosol extinction is zero, $\alpha_a(z_0) = 0$. In our case, $z_0 = 7$ km. The atmospheric extinction at this normalisation height, $\alpha_{atm}(z_0)$ is then given by $\alpha_{atm}(z_0) = \alpha_m(z_0) = S(z_0)\beta_m(z_0)$. The normalisation height should be defined carefully, so that there is still a good value of Signal-to-Noise-Ratio (SNR) but that there can be stated with high certainty that it is a height free of aerosols.

In our calculations for the AOD, following the Klett procedure, the value for S is defined to be height dependent. From literature (Wandinger, Ulla et al., 2016; Greatwood et al., 2017) and from the observations on the island, it is concluded that marine aerosols are always present in the lower boundary layer, up until 1200 m. S_{marine} is set to be 25 sr, a good approximation for marine aerosols (Wandinger, Ulla et al., 2016; Cattrall et al., 2005; Müller et al., 2007). (Aged) Smoke and dust is often, almost always, present above the boundary layer, in the layer from 1200 m to 5000 m, sometimes it can be mixed in the boundary layer. S_{dark} is defined to be the value used for the aerosol-to-extinction coefficient in this layer. This is just a definition in this study for the coefficient used where smoke and dust are the most likely aerosols. S_{dark} is set to 50 sr, which is an appropriate value for dust and aged biomass burning aerosols (Wandinger, Ulla et al., 2016). Above 5000 m, the air was mostly clean and clear of aerosols, the lidar ratio is set to be the molecular extinction-to-backscatter ratio, $S_{\text{mol}} = \frac{8\pi}{3}$ sr (Guzzi, 2008, p. 231). The marine particle and aerosol extinction-to-backscatter ratios can be different than assumed and can therefore cause an error, this error will act as a bias error, and is evaluated in the next chapter, by varying S_{marine} and S_{dark} around the values of 25 and 50 sr. To check if the correct values are chosen, also in situ data about the type of aerosols can be used.

The lidar equation, (3.1), is rewritten to a two-component lidar equation for cloud-free situations. In this two-lidar equation, the signal is first corrected for the molecular transmission, and the lidar-ratio is included from the equation $\beta(z) = \frac{\alpha(z)}{S(z)}$. Transformed variables are introduced: $P'(z) = S(z)P(z)e^{2\int_0^z (\alpha_m(z') - S(z')\beta_m(z'))dz'}$ and $\alpha'(z) = (S(z)\beta_m(z) + \alpha_a(z))$, which results in:

$$P'(z) = \frac{C_{lid}}{z^2}\alpha'(z)e^{-2\int_0^z \alpha'(z')dz'} \tag{3.2}$$

$P'(z)$ and α' are the transformed variables for the rewritten lidar signal equation in height z. C_{lid} is the lidar calibration constant. With the definition $\tau' = \int_0^{z_0} \alpha'(z')dz'$

the transformed lidar equation is rewritten and differentiated which gives:

$$\alpha'(z) = \frac{d\tau'}{dz}(z) = \left[\frac{P'(z)z^2}{C_{lid} - 2\int_0^z P'(z')z'^2 dz'}\right] \tag{3.3}$$

This is transformed into a boundary value problem:

$$\alpha'(z_0) = \left[\frac{P'(z_0)z_0^2}{C_{lid} - 2\int_0^z P'(z')z'^2 dz'}\right] \tag{3.4}$$

with $P'(z_0)$ the transformed lidar signal at the normalisation height, $\alpha'(z_0)$ the transformed extinction at the normalisation height, which is a known value: $\alpha'(z_0) = (S(z_0)\beta_m(z_0) + \alpha_a(z_0))$ because the assumption is that $\alpha_a(z_0) = 0$ at the normalisation height and $S(z_0)$ and $\beta_m(z_0)$ are both known values. At $z = z_0$, $S(z_0) = S_{\text{mol}} = \frac{8\pi}{3}$ sr and $\beta_m(z_0)$ is calculated from the Rayleigh scattering. Equation (3.4) solved for C_{lid} and filled in in equation (3.3) gives the solution for the transformed variable $\alpha'(z)$:

$$\alpha'(z) = \left[\frac{P'(z)z^2}{\frac{P'(z_0)z_0^2}{\alpha'(z_0)} + 2\int_z^{z_0} P'(z')z'^2 dz'}\right] \tag{3.5}$$

From the transformed variable α' the aerosol extinction is derived to be $\alpha_a(z) = \alpha'(z) - S(z)\beta_m(z)$. The aerosol backscatter coefficient is now derived by dividing the aerosol extinction by the height dependent lidar ratio. To calculate the AOD, the aerosol extinction coefficient is integrated over the vertical column, $\tau = \int_0^{z_{\max}} \alpha_a(z)dz$, where z_{max} is a chosen value for the maximum height to integrate the extinction over. This maximum height is in our study 1000 m above the normalisation height, and thus 8 km.

3.1.3. Cloud parameters retrieval

Four out of the six atmospheric unknowns in equation (3.1) have now been treated. For the derivation of the cloud extinction and backscatter coefficient, a different approach is necessary because the lidar equation only applies when no multiple-scattering is accounted for. Multiple-scattering is taken into account in the Monte Carlo (MC) optimal estimation method.

With this method, and most already existing cloud parameter retrieval methods, cloud parameters can be derived only for a liquid water cloud, with a (quasi-) linear liquid water content (LWC) and a (quasi-) constant cloud droplet number concentration (N_d). The cloud droplet size distribution used in this method, is defined as a single-mode modified-gamma distribution (Miles et al., 2000):

$$n(R) = \frac{N_d}{R_m}\frac{1}{(\gamma-1)!}\left(\frac{R}{R_m}\right)^{\gamma-1}\exp\left(\frac{R}{R_m}\right), \tag{3.6}$$

where N_d is the cloud droplet concentration, defined to be constant with height, R is the droplet radius, R_m is the so-called mode radius and γ is the shape parameter of the distribution.

The method is based on multiple scattering by the liquid water cloud droplets. The returning light from the cloud will be partially depolarised due to multiple scattering (Liou and Schotland, 1971). This multiple scattering on the liquid water clouds defined by the cloud model is simulated by Monte Carlo (MC) modelling. The MC model used is the Earth Clouds and Aerosol Radiation Explorer (EarthCARE) simulator (ECSIM) lidar-specific MC forward model. The ECSIM lidar MC model is a modular multi-sensor simulation framework, which in our case can calculate the spectral-polarisation state of the lidar signal. The ECSIM lidar MC model is shortly described in appendix B.1. An in depth explanation about the MC model and the method in general can be found in D. P. Donovan et al. (2015).

The constraints on the LWC and N_d as given before, are met in the simple cloud representation described by Roode and Los (2008). With this cloud model, the parameters to describe the cloud are reduced to two, the cloud effective radius (R_{eff}) and the cloud extinction (α_c). A linear liquid water content defines a constant liquid water lapse rate, Γ_l. When the liquid water content increases with height and the number density remains constant, R_{eff} will increase with height. The cloud extinction coefficient, α_c, also increases with height. Be aware that the clouds in the MS based inversion method are represented by semi-infinite clouds, with a cloud top at infinity because the lidar can only penetrate a few hundred meters into the cloud, no information is known about the upper part of the cloud. This leads to the prediction that the depolarisation ratio is generally increasing throughout the cloud, while observations show that the depolarisation ratio may exhibit a peak (Sassen and Petrilla, 1986).

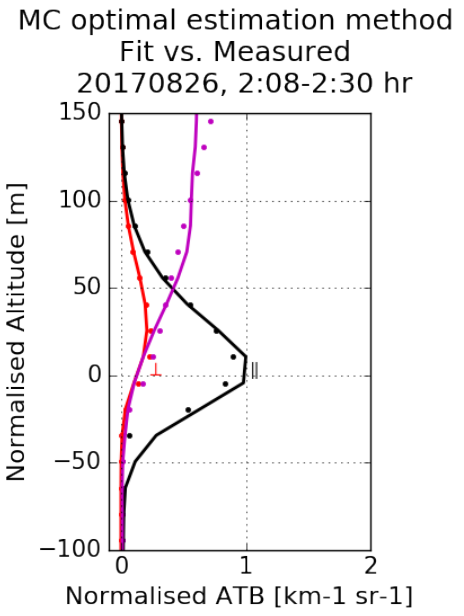

Figure 3.2: A step in the MS based inversion method. The measured data is shown by the lines, the dots show the fitted profiles, used in the method. Black for the parallel ATB, red for the perpendicular ATB and magenta for the depolarisation ratio.

These parameters are calculated for a reference height. The lidar signal will not penetrate further into the cloud than 100-300 m, so the retrieved parameters are only applicable to the cloud-base region. For the reference height, in this research, 100 m above cloud-base is used. The parameters used in this research are therefore R_{eff}^{100}, R_{eff} at reference height, and α_c^{100}, α_c at reference

height.

The MC simulations were performed for various values of the cloud-base height, the lidar field-of-view (FOV), R_{eff}^{100} and Γ_l. The exact values can be found in Table 1 in D. P. Donovan et al. (2015) and in table B.1. Look-up tables (LUTs) were generated from the simulations and predefined input parameters, the lidar constants and initial values for R_{eff}^{100} and α_c^{100}. These LUTs contain information on the simulated parallel and perpendicular ATB and therefore the depolarisation ratio.

The Cloud Base Height (CBH) is difficult to define from real observation due to the presence of sub-cloud drizzle and the presence of growing aerosol particles. The need to accurately identifying the CBH directly from observations is avoided by using the peak of the observed parallel lidar ATB as a reference instead of the CBH in the fitting procedure. The CBH is produced as a product of the fitting procedure determined by the optimal fit to the observations, which is used to define R_{eff} 100 m above the CBH. The observed ATB and depolarisation ratio are compared to the LUTs, by an iterative process, to find the best matching values for R_{eff}^{100} and α_c^{100}. After the simulated profiles, which are normalised by the maximum value of the observed parallel ATB, the best fit out of the simulations can be found by minimizing a cost-function as given in (Rodgers, 2000, p. 238). In this procedure the best fit for a distinct pair of the R_{eff}^{100} and α_c^{100} with the observed profiles is found in the LUTs. An estimate of the cloud-base height is a by-product of the fitting procedure determined by the optimal fit to the observations. In figure 3.2, the observed and fitted ATBs and depolarisation ratio profiles from the LUTs are shown, for a cloud selection on the 26th of August, shown in figure 3.1. The scatter plots correspond to the fitted values from the LUTs, with the parallel ATB in black, the perpendicular ATB in red and the depolarisation ratio in magenta. The observed value for the parallel ATB is shown by the black line, the perpendicular ATB by the red line and the depolarisation ratio by the magenta colored line.

Because multiple-scattering is occurring in a cloud, the LUTs, the shape of the ATB profiles and the depolarisation ratio are all well-defined functions of the LWC and effective radius profile. For single-scattering the parallel ATB profile will not depend on the effective radius profile.

To summarize, the inversion scheme to define the values for the cloud parameters from the observed parallel and perpendicular ATB and the depolarisation ratio, is based on finding the best fit for the normalised ATBs by finding a global minimum in the cost-function, regarding the simulated LUTs. Care should be taken; local minima in the cost function can exist, errors in the depolarisation calibration (e.g. C_{r} and δ^{C}) need to be taken into account, and because normalised ATB is used, the error in the normalisation should also be accounted for. The calibration constants are defined a priori for the methods, with different values in both years after analyzing the lidar depolarisation in cases of only Rayleigh scattering.

3.2. Cloud parameters from other instrumentation

The instruments we used from the ARM site to retrieve cloud products for our intercomparison were the cloud radar and the microwave radiometer. To retrieve the same product as retrieved with the lidar, R_{eff}^{100}, 2D reflectivity data and the LWP from the cloud radar and the MWR, respectively, were used. In figure 3.3 a time-height cross section of the radar reflectivity from the KASACR is shown for a cloud selection. The reflectivity factor from the ARM dataset is given in decibel, dBZ. $\text{dBZ} = 10\log(\text{Z}) + 180$ to translate it to the reflectivity factor Z in $\text{m}^6\,\text{m}^{-3}$.

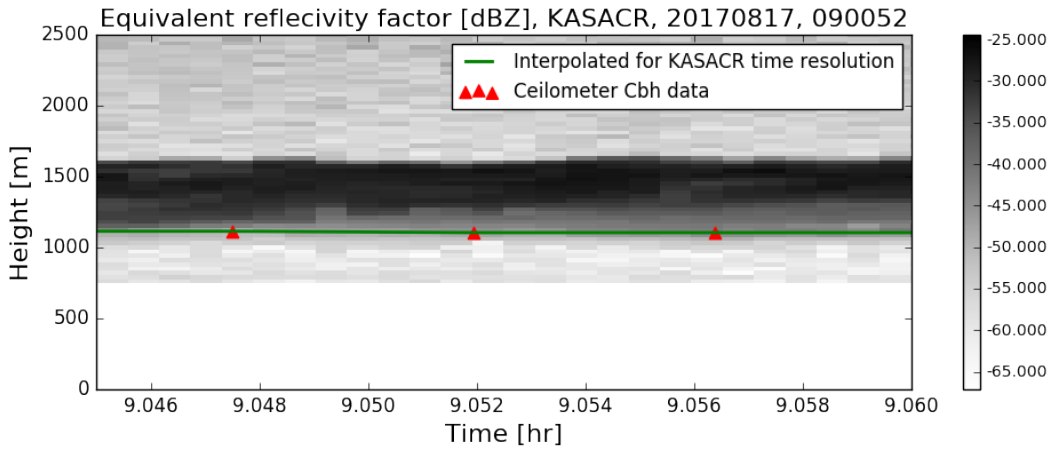

Figure 3.3: A step in the cloud parameter retrieval following Frisch's method with the cloud radar data (Frisch, Shupe et al., 2002). The reflectivity factor, as a contour plot, with the measured cloud base from the ceilometer plotted with the triangles, the green line represents the interpolated cloud base height to the radar time resolution.

To retrieve the R_{eff}^{100} from the ARM instrumentation, two methods described by Frisch (Frisch, Fairall et al., 1995; Frisch, Shupe et al., 2002) were used. One where a constant cloud droplet number concentration (N_d) throughout the cloud is set, which gives a relationship for the R_{eff}^{100} only depending on the reflectivity factor. The second method uses the LWP as additional input, which makes the assumption for N_d unnecessary. This second method gives a relationship between the LWP, reflectivity factor and R_{eff}, and is for example used by Sarna and Russchenberg (2016) in a new approach to study ACIs. Both methods are fully described in Frisch, Shupe et al. (2002).

In both methods, a lognormal model of the cloud droplet size distribution is used. The mean value and the spread of the lognormal distribution needs to be assumed a priori. For our retrievals the droplet spread is set on an assumed value of 0.34, to be a good assumption for the spread in marine, low-level stratocumulus clouds, taken from literature (Fairall et al., 1990; Frisch, Fairall et al., 1995; Miles et

al., 2000). This lognormal spread for the cloud droplet size distribution, is varied to analyze the uncertainty from this parameter on R_{eff}. The lognormal cloud droplet size distribution used in the retrieval is given by:

$$n(R) = \frac{N_d}{\sqrt{2\pi} R \sigma_x} \exp\left[\frac{-(\ln(R) - \ln(R_0))^2}{2\sigma_x^2}\right], \tag{3.7}$$

where N_d is the cloud droplet concentration, defined to be constant with height, R is the droplet radius, R_0 is the median radius, and σ_x is the logarithmic spread of the distribution. In a lognormal droplet size distribution R_{eff} is related to the median radius by $R_{\text{eff}} = R_0 \exp(\frac{5}{2}\sigma_x^2)$ and the radar reflectivity factor for a lognormal cloud droplet size distribution is $Z = 2^6 N_d R_0^6 \exp(18\sigma_x^2)$. Solved for R_{eff}, this gives retrieval method 1:

$$R_{\text{eff}} = \frac{1}{2}\left(\frac{Z}{N_d}\right)^{1/6} \exp(-0.5\sigma_x^2). \tag{3.8}$$

From equation (3.8), it is clear that relatively large changes in the cloud droplet concentration N_d or in the logarithmic spread σ_x, will only produce small changes in R_{eff}. This is why, if we have an estimate of N_d and σ_x, R_{eff} can be retrieved from Z.

The radar retrievals were executed in two ways, with different assumptions for N_d. One were a constant value of 100 cm^{-3} was set, which was taken from literature for low-level marine stratocumulus clouds (Davidson et al., 1984; Martin et al., 1994). The other implementation was with a daily varying value for the a priori definition of N_d, gathered from the lidar retrievals. Besides R_{eff}, the MS based inversion method also has N_d as a product. This product was daily averaged and these values were used as input for the assumption on N_d in Frischs method 1. This first method is executed to retrieve the effective radius data for the 2016 and 2017 measurement periods.

For the 2016 retrievals, LWP data is available online, so the second method was also performed. The derivation of equation (3.9), for R_{eff} as a function of height, can be found in Frisch, Shupe et al. (2002).

$$R_{\text{eff}}(h) = \frac{Z^{1/6}(h)}{2\text{LWP}^{1/3}} \left(\frac{\pi\rho}{6}\right)^{1/3} \left(\sum_{i=1}^{i=m} Z^{1/2}(h_i)\Delta h\right)^{1/3} \exp(-2\sigma_x^2) \tag{3.9}$$

N_d and σ_x are again constrained to be constant in height, h_i is the height in the cloud, $i = 1$ is the radar range gate at cloud base, derived from ceilometer data on the main ARM site. $i = m$ represents the radar range gate at cloud top. The radar range gate at cloud top is found to be the highest range gate where the reflectivity factor is higher than -44 dBZ, which seemed appropriate for our retrievals. Δh is the radar range gate thickness, 30 m in our case, ρ is the water density, 10^6 g m^{-3}. The LWP is the microwave radiometer-derived integrated liquid water content in g m^{-2}. This second method eliminates the assumption on N_d.

The WSACR was only operating until the 12th of September in 2016. As the LWP has an uncertainty of 15 $\mathrm{g\,m^{-2}}$ calculated from the MWR (Turner et al., 2007), the values below 30 $\mathrm{g\,m^{-2}}$ are disregarded. In marine stratocumulus clouds, drizzle can appear from 90 $\mathrm{g\,m^{-2}}$ (Rémillard et al., 2012), so the values above 90 $\mathrm{g\,m^{-2}}$ are also excluded from the retrievals. Only the values between 30 and 90 $\mathrm{g\,m^{-2}}$ are used for the retrieval with Frischs method 2.

The uncertainties in the retrieval from the assumptions and measurement errors in both methods are described in Frisch, Shupe et al. (2002). In the first method, where R_{eff} is only depending on the assumptions for N_d, σ_x and the measurements of the reflectivity factor, the error in R_{eff} can be calculated with equation 7 in Frisch, Shupe et al. (2002). In method 2, the method with the LWP data points, there is no longer an error due to N_d, but there is an error due to the measurement error of the LWP, which is assumed to be 20% (Westwater et al., 2001). The final retrieval error in R_{eff} is calculated with equation 9 in Frisch, Shupe et al. (2002).

4. Results

4.1. Lidar data processing

To retrieve the AOD and the cloud parameters from the lidar data, the measured attenuated backscatter (ATB) was analyzed with the Klett inversion method and the MS based inversion method respectively. With the results that are shown and described, the uncertainties were also evaluated. The results are analyzed in comparison with the retrieved products from other instruments and from other methods, as described in the previous chapter. This provides an outlook on the validation of our retrievals.

Correction for misalignment in 2017

The lidar itself causes uncertainties in the measurements, instrument errors. In 2017 the laser beam was slightly misaligned, therefore less power was detected by the receiver, the SNR was lower and larger uncertainties arise due to the uncertainties in the calibration coefficients, C_r and δ^{C}. The calibration coefficients need to be defined a priori, and were in 2017 corrected for this misalignment, the used values in both measurement periods are shown in table 2.2. In the estimation of the calibration coefficients for 2017, the uncertainty is large because of an assumption for the effect of the misalignment. After the corrections in the calibration coefficients, the consistency in the lidar operation over the two measurement periods was evaluated by analyzing the depolarisation ratio in both years at moments of no clouds, and altitudes without aerosols. These selections were made by a visual inspection of the raw data, and are generally of a height bin of 1 km thick and above a height of 5 km. The results of the averaged depolarisation ratio in these boxes for both measurement periods are shown in A.1. The average depolarisation ratio over the two measurement periods differs slightly but not significantly to expect the lidar to operate differently, after the correction. We do see that the standard deviations in the values for the depolarisation ratio differ by a significant factor, this is due to lower SNR in 2017 and therefore larger variation in the signal. From the results it seems that the instrument calibration, after the correction in the calibration coefficients for 2017, is consistent over both measurement periods.

In the aerosol retrievals and AOD calculations, the misalignment will be noticeable because of the lower SNR, and therefore larger standard deviations when averaging. In the cloud product retrieval, the correction for the misalignment in the calibration coefficients was of importance, in addition to the low SNR. And also, a correction was made on the look-up tables (LUTs) for the misalignment because this misalignment mostly affected the multiple-scattering (MS) and therefore the

fitting procedure of the LUTs with the observed depolarisation ratio. This correction is only mentioned here, no further consequences are taken into account.

4.2. AOD

The lidar retrieved AODs are analyzed for both periods taking into account the systematic error arising from the definition of the extinction-to-backscatter ratios and the random error due to the definition of the normalisation height. The results are shown in figure 4.2(a) and 4.3(a). The retrieval errors due to the extinction-to-backscatter ratio $S(z)$ and the normalisation height z_0 are evaluated in the next paragraphs and shown in the figures 4.2(b), 4.2(c) and 4.3(b), 4.3(c). The results are compared to the AOD data from AERONET, the Microtops and the Calitoo. The intercomparisons are shown in figure 4.2(d) and 4.3(d). Striking cases after this intercomparison were evaluated and an interpretation for the aerosol vertical distribution is made.

4.2.1. AOD retrieval from lidar data

Uncertainty due to the assumption for $S(z)$

The standard assumed values for the retrieval of the AODs were described in the previous chapter to be $S_{\text{marine}} = 25$ sr, $S_{\text{dark}} = 50$ sr, $S_{\text{mol}} = \frac{8\pi}{3}$ sr, $z_0 = 7000$ m and $z_{\text{max}} = 8000$ m. The results of the AOD retrieval for both years with these standard values is shown in figures 4.2(a) and 4.3(a). To define the possible bias error from the uncertainty in $S(z)$, the values for S_{marine} and S_{dark} were varied and the AODs were calculated. The marine particle extinction-to-backscatter ratio, S_{marine} (for the 0 m to 1200 m altitude domain) was varied in the range 20-30 sr and the 'dark' aerosol extinction-to-backscatter ratio, S_{dark} (for the 1200 m to 5000 m altitude domain) was varied in the range 40-60 sr. The uncertainties resulting from varying the ratios are shown in figures 4.2(b) and 4.3(b). The shaded area represents the results from varying over the ranges for S_{marine} and S_{dark}. The lower boundary represents the AODs calculated for the combination with the lowest values of $S(z)$, $S_{\text{marine}} =$ 20 sr and $S_{\text{dark}} = 40$ sr. The upper boundary represents the AODs calculated for the combination with the highest values of $S(z)$, $S_{\text{marine}} = 30$ sr and $S_{\text{dark}} = 60$ sr. The exact averaged values for the AODs over the measurement periods, with nine combinations for the varying of the ratios, are shown in appendix A.2.

The average AOD in 2016 calculated for the standard values for the retrieval was 0.26$\pm$0.116 as we saw in figure 4.2(a). The average AOD is 0.236$\pm$0.11 for the combination of S with the lowest values and 0.281$\pm$0.121 with the combination of S with the highest values. In 2016 a change of 20 % in the initial values of the extinction-to-backscatter ratios gives a change of 8.7 % in the average AOD value. For 2017 the average AOD for the standard extinction-to-backscatter ratios was 0.27$\pm$0.132, as we saw in figure 4.3(a). The average AOD varies to 0.247$\pm$0.126

and 0.288±0.136 for a change in the values for the extinction-to-backscatter ratios to the lowest or highest combination respectively. So a change of 20 % in the initial values of S gives a change of 7.6 % in the final average AOD value in 2017. Despite the lower SNR and larger standard deviations in 2017, the uncertainty due to the estimation of S is slightly larger in 2016.

Uncertainty due to the assumption for z_0

Another uncertainty in the AOD retrieval is the definition of the normalisation height z_0. To analyze this uncertainty, z_0 is varied to 6500 m and 7500 m in the Klett inversion method. The results for both years, with the standard values for the extinction-to-backscatter ratios and the varying normalisation height, is shown in figures 4.2(c) and 4.3(c). In the Klett inversion method the total lidar backscatter is defined for this normalisation height to solve the boundary value problem. For the total lidar backscatter at this normalisation height the average of 5 range gates (75 meters) of the lidar is calculated. So we look at the effect of varying the altitude for the normalisation height on the value for the total lidar backscatter which is used for the boundary value problem and which is influenced by the height-resolved signal, the assumption of the aerosol free altitude and the noise. The maximum height for the integration of the extinction profile, to calculate the AOD, varies with the same absolute value as the variation in the normalisation height.

The average AOD in 2016 calculated for the standard values for the retrieval was 0.26±0.116 as we again saw in figure 4.2(a). The average AOD in 2016 is 0.25±0.117 for z_0=6500 m and 0.262±0.129 for z_0=7500 m. A variation in normalisation height of 500 m, 7 %, and therefore a change in the value for the signal assumed to be at the aerosol free altitude, gives an average change of 2.3 % in the final averaged AOD value in 2016. For 2017 the average AOD for the standard normalisation height of 7000 m was 0.27±0.132, as we saw in figure 4.3(a). The average AOD varies to 0.287±0.18 and 0.239±0.19 for z_0=6500 m and z_0=7500 m respectively. A variation in normalisation height of 500 m, 7 %, and thus a change in the signal assumed to be at aerosol free altitude, gives a change of 8.9 % in the final averaged AOD value in 2017. The uncertainty due to the estimation of the normalisation height, and therefore the estimation of the signal at aerosol free altitude used in the boundary value problem, is larger in 2017, due to the lower SNR.

Total uncertainty

The AODs are more sensitive to the definition of the normalisation height then to the definition of the values for the extinction-to-backscatter ratios. And as we see from figures 4.2(b) and 4.3(b), varying $S(z)$ gives a systematic uncertainty, while varying z_0 gives a random uncertainty, which we can see in figures 4.2(c) and 4.3(c). The retrieval (instrument) error due to the uncertainties in $S(z)$ and z_0 is 11 % in 2016 and 16.5 % in 2017. Next to the retrieval error, random uncorrelated errors in

the signal are taken into account, the standard deviation in the selections, which were shown with the error bars in figures 4.2(a) and 4.3(a). This standard deviation is 7.5 % on average in 2016 and 10.4 % on average in 2017. So the total uncertainty of the AOD, random plus systematic, averaged over the measurement periods is 18.5 % in 2016 and 26.9 % in 2017.

4.2.2. Study cases AOD calculation

The clear sky selection for which the dependency on the normalisation height is the largest, is now examined in detail. This selection is on the 25th of August 2017, as can be seen in figure 4.3(c). This is due to the low SNR, which can be seen in figure 4.1(a). To see the difference in 2017, the averaged ATB for a case on the 26th of August 2017 is shown in figure 4.1(b). The ATB has a larger SNR than the selection on the day before, and therefore the AOD is not as sensitive to the definition of z_0. The different time in the days for the selections can be the cause of this difference in SNR, because from around 8 AM, direct sunlight will lower the SNR. The averaged ATB for one selection in 2016, on the 14th of September, is shown in figure 4.1(c). The averaged ATB has an even smaller standard deviation and thus the calculated AOD is less dependent on the definition of z_0, which we could also conclude from figure 4.2(c) is the case for 2016 on average.

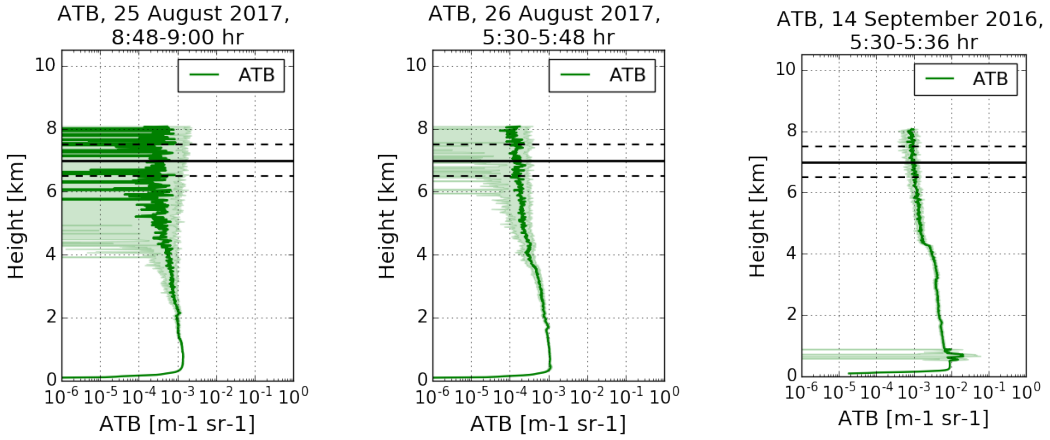

(a) (b) (c)

Figure 4.1: The averaged ATB for three selections. One on the 25th of August 2017 (a), one on the 26th of August 2017 (b) and one on the 14th of September 2016 (c). The shading is the standard deviation. The black line shows $z_0 = 7000$ m, the standard value. The dashed lines show $z_0 = 6500$ m and $z_0 = 7500$ m.

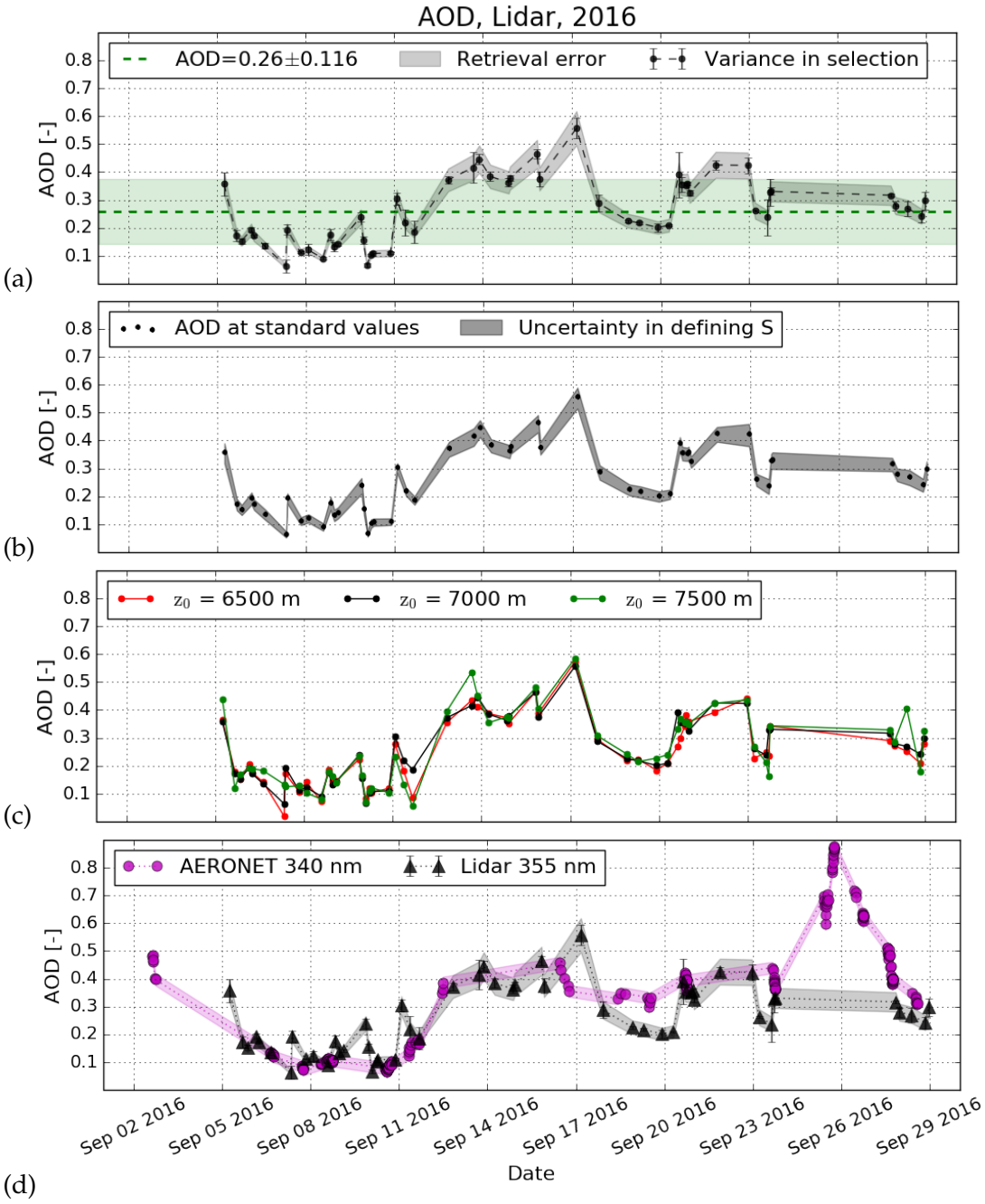

Figure 4.2: In (a) The AODs for the clear sky selections in the 2016 measurement period are shown. With the error bars, the standard deviation of the AOD is shown. The errors calculated for the AOD come from the integrated random uncorrelated errors in the extinction profile. The shaded area shows the retrieval error, 11 %. The average AOD during the measurement period is shown by the green dashed line, the shading around this line is the variation around this mean value, the standard deviation. In (b) the AODs for varying values of $S(z)$, the aerosol extinction-to-backscatter ratio is shown. The dots are the AOD calculated with the standard values for $S(z)$, $S_{\text{marine}} = 25$ sr and $S_{\text{dark}} = 50$ sr. The lower boundary represents the AOD for $S_{\text{marine}} = 20$ sr and $S_{\text{dark}} = 40$ sr. The upper boundary represents the AOD for $S_{\text{marine}} = 30$ sr and $S_{\text{dark}} = 60$ sr. In (c) the AODs for varying values of z_0, the normalisation height, is shown. The black line represents the AODs calculated with the standard values for $S(z)$ and z_0. The red line shows the results for $z_0 =$ 6500 m and the green line shows the results for $z_0 = 7500$ m. (d) shows the AODs retrieved with the lidar and the AODs from AERONET. The black error bars show the standard deviation of the lidar retrieved AODs. The shaded areas show the retrieval errors, 0.021 for the AERONET data and 11 % for the lidar data.

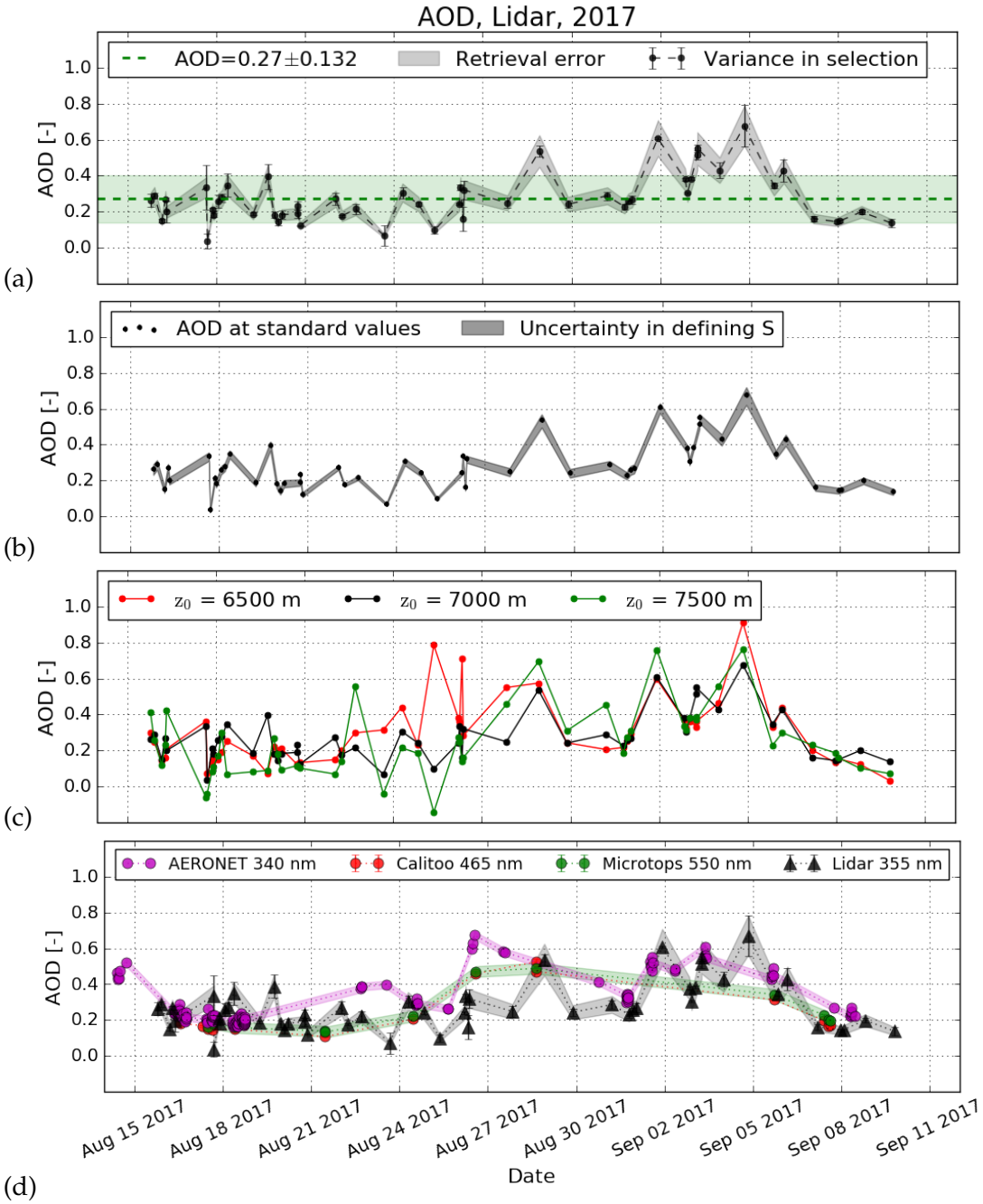

Figure 4.3: In (a) The AODs for the clear sky selections in the 2017 measurement period are shown. With the error bars, the standard deviation of the AOD is shown. The errors calculated for the AOD come from the integrated random uncorrelated errors in the extinction profile. The shaded area shows the retrieval error, 16.5 %. The average AOD during the measurement period is shown by the green dashed line, the shading around this line is the variation around this mean value, the standard deviation. In (b) the AODs for varying values of $S(z)$, the aerosol extinction-to-backscatter ratio is shown. The dots are the AOD calculated with the standard values for $S(z)$, $S_{\text{marine}} = 25$ sr and $S_{\text{dark}} = 50$ sr. The lower boundary represents the AOD for $S_{\text{marine}} = 20$ sr and $S_{\text{dark}} = 40$ sr. The upper boundary represents the AOD for $S_{\text{marine}} = 30$ sr and $S_{\text{dark}} = 60$ sr. In (c) the AODs for varying values of z_0, the normalisation height, is shown. The black line represents the AODs calculated with the standard values for $S(z)$ and z_0. The red line shows the results for $z_0 = 6500$ m and the green line shows the results for $z_0 = 7500$ m. (d) shows the AODs retrieved with the lidar and the AODs from AERONET, the Calitoo Aerosol photometer and the Microtops. The error bars show the standard deviation of the retrieved AOD. The shaded areas show the retrieval errors, 0.03 for the Microtops, 0.021 for the AERONET data and 16.5 % for the lidar data. For the Calitoo no retrieval error is indicated.

To check whether the uncertainty due to the definition of the normalisation height can be decreased, a larger altitude domain is chosen to average over for the normalisation height. In figure 4.4(b) the results of the Klett inversion method are shown for the 2017 measurement period, when for the normalisation height an altitude domain from 6000 to 7000 m is used. The assumption is that the altitudes above 6000 m are free of aerosols, which was the case in 2017. By averaging over such a large amount of range gates, we see that the standard deviations in the selections decrease, the average standard deviation for the selections is 3.5 % instead of the 10.4 % which was the case for the results with the normalisation height averaged over 5 range gates, as used as standard amount in the Klett inversion method. To use this altitude domain instead of the standard normalisation height averaged over only 5 range gates, the modification should first be studied in more detail.

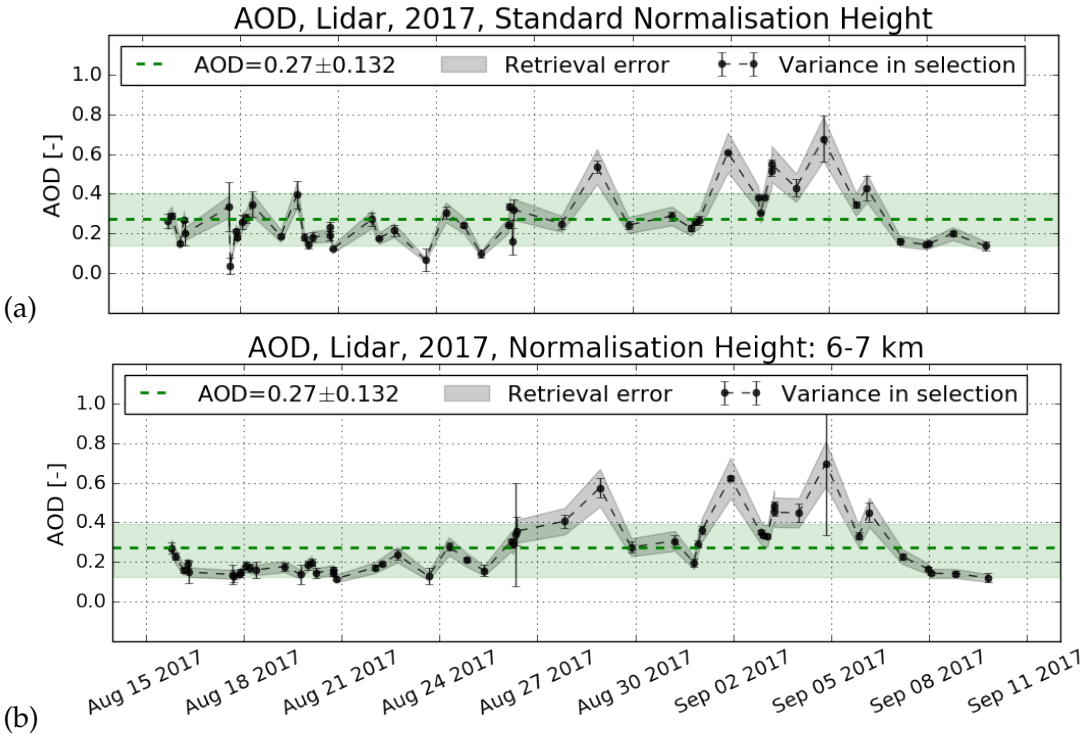

Figure 4.4: In (a) The AODs for the clear sky selections in the 2017 measurement period are shown, with the standard value of $z_0 = 7000$ m. And the average of 5 range gates around that altitude. These results are the same as shown in 4.3(a). In (b) the AODs for the clear sky selections in the 2017 measurement period are shown with the normalisation height chosen to be the altitude domain from 6000 up to 7000 m. This means 66 range gates are averaged over for the power at the normalisation height. In both figures: with the error bars, the standard deviation of the AOD is shown. The errors calculated for the AOD come from the integrated random uncorrelated errors in the extinction profile. The shaded areas show the retrieval error, 16.5 %. The average AOD during the measurement period is shown by the green dashed line, the shading around this line is the variation around this mean value, the standard deviation.

We see two data points with large standard deviations in the results from the Klett inversion method with the averaging for the normalisation height over an altitude domain of 1 km. The selection with the largest standard deviation, on the 4th of September 2017, I now look at in further detail. The averaged ATB for the selection is shown in figure 4.5(a). With the gray band, the normalisation height domain is indicated. The standard deviation for the extinction profile is large probably because of liquid water present in the boundary layer, which we can see from the averaged ATB profile and we will check with the quicklook of the raw data in figure 4.5(b). Indeed high signals for the total lidar backscatter are seen at the start of the averaging interval. This points out that clear-sky selections should be defined with care, which was not the case for the two selections in the 2016 measurement period as we saw now. The other selections are well defined clear-sky selections and therefore we can overall trust the selections. By using the altitude domain of 1 km for the normalisation height, the standard deviation overall decreases, because noise is averaged out better. In the cases were the standard deviation increases, noise is not the cause of the large variation, so probably liquid water is present in the vertical profile which causes large uncertainties. This averaging over a larger altitude domain was only done to see the consequences, further research needs to be done to verify whether this change can be made for the Klett inversion method to give better accuracy. The use of an altitude domain of 1 km for the normalisation height could be used to better select the cloud-free periods.

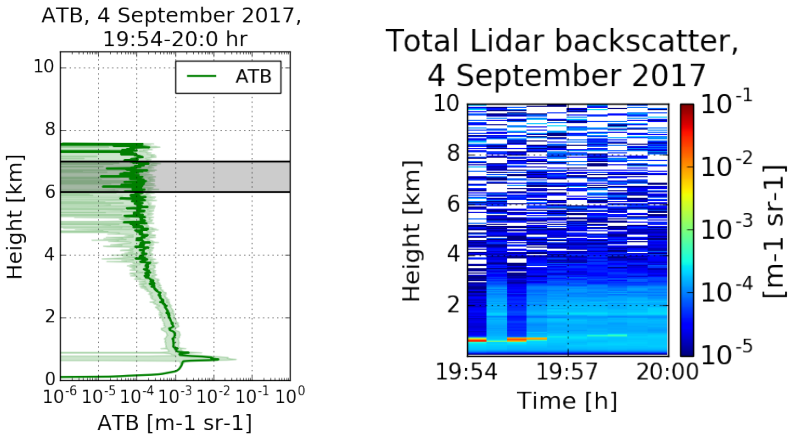

Figure 4.5: One clear-sky selection on the 4th of September 2017. The averaged ATB from the lidar signal in (a). The shading is the standard deviation. The black lines show the limits of the normalisation altitude domain, 6000 and 7000 m. The total lidar backscatter, raw data, for the selection is visualized in (b).

4.2.3. AOD intercomparison

AERONET data was used to compare our lidar retrievals with for the 2016 measurement period. In 2017 the AOD was also measured with the Calitoo and with the Microtops from the CLARIFY campaign. So for the 2017 measurement period our lidar retrieved AODs were compared to the AERONET, Calitoo and Microtops data. The results are shown in figures 4.2(d) and 4.3(d).

The AERONET data has an instrument uncertainty of 0.021 at 340 nm. The Microtops have an accuracy of 0.03 for the 550 nm measurements. In addition to the instrument uncertainty, the Microtops data was averaged over measurements gathered within 5 minutes, which gives a standard deviation of 0.0033 on average. This averaging was also done for the Calitoo measurements, which gives an average uncertainty of 0.0063. The instrument uncertainties are shown with the shadings in figures 4.2(d) and 4.3(d), the variation in the measurements within 5 minutes is shown with the error bars.

The AODs were measured at different moments in time for the different instruments. Cloud-free periods selected for the lidar data do not mean that AERONET data is measured at that specific moment because clouds can be present above the main ARM site where the AERONET sun-photometer was positioned. All of the AOD measurements are done within a spatial range of 5 km from the lidar, this is close enough to assume that the aerosol distribution will be comparable for the measurements within this spatial range (Carlson and Prospero, 1972; Zuluaga et al., 2012), if the time separation of the measurements is no more than a day. As the aerosol distribution will be quite stable over a time range of a day, averaging over a day gives results which can be compared. That is why in figures 4.6 and 4.7 the average values per day, for all the instruments, are compared.

The square of the correlation coefficients, r-squared, is given in the legends. For 2016, the daily averaged AODs we retrieved with the lidar agree within the uncertainty with the daily averages from AERONET, with an r-squared of 0.76. But there is an offset between the two of about 36 %, the AERONET data increases relative to the lidar data with increasing AOD values. In 2017, there is more variation and uncertainty in the lidar retrieved AODs as we saw already in figure 4.3(a). A small correlation, r-squared is 0.29, between the lidar retrieved AODs and the data from AERONET is found. This small correlation is influenced much by the three datapoints in the upper left of figure 4.6(b). The cause of the significant deviation of such a data-point is shown later.

As we can see in figure 4.7, the Microtops measured AOD values correlate well with the Calitoo measured AODs (4.7(a)) and the Calitoo measured AODs correlate well with the AERONET AODs (4.7(b)). Although there is an offset between the AERONET data and the Calitoo data of around 40 %. As can be seen in figure 4.7(c), with a value of 0.53 for the r-squared, the lidar retrieved AODs correlate well with the Calitoo measured AODs.

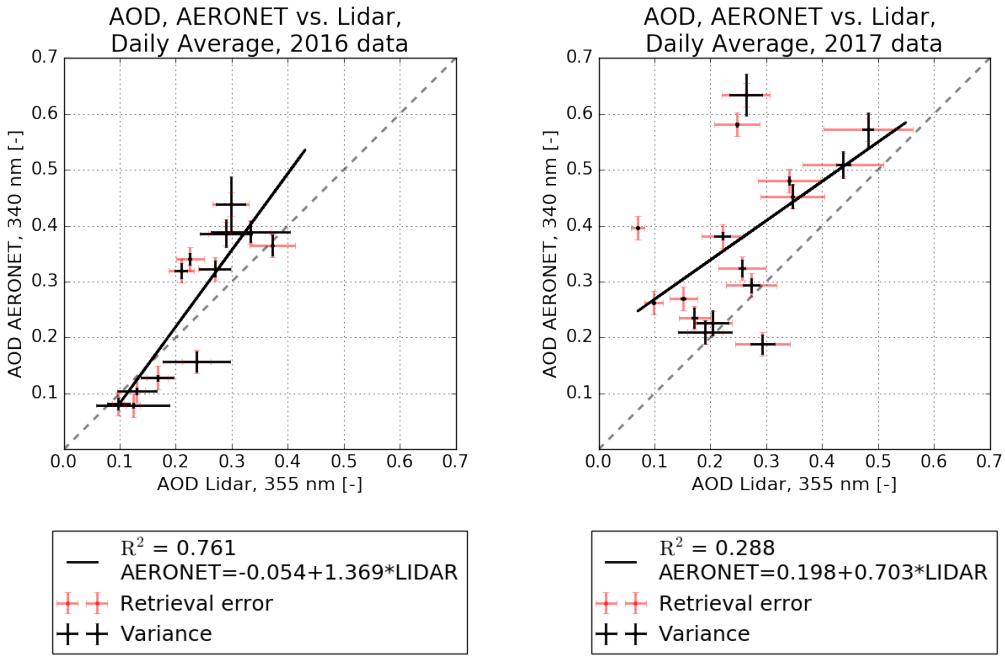

(a) (b)

Figure 4.6: For both measurement periods the daily averaged AOD values retrieved with the lidar are compared to the daily averaged AOD values from AERONET. The black error bars show the variation around the calculated mean value per day. The red error bars show the retrieval error, 0.021 for the AERONET data, 11 % for the lidar data in 2016 and 16.5 % for the lidar data in 2017.

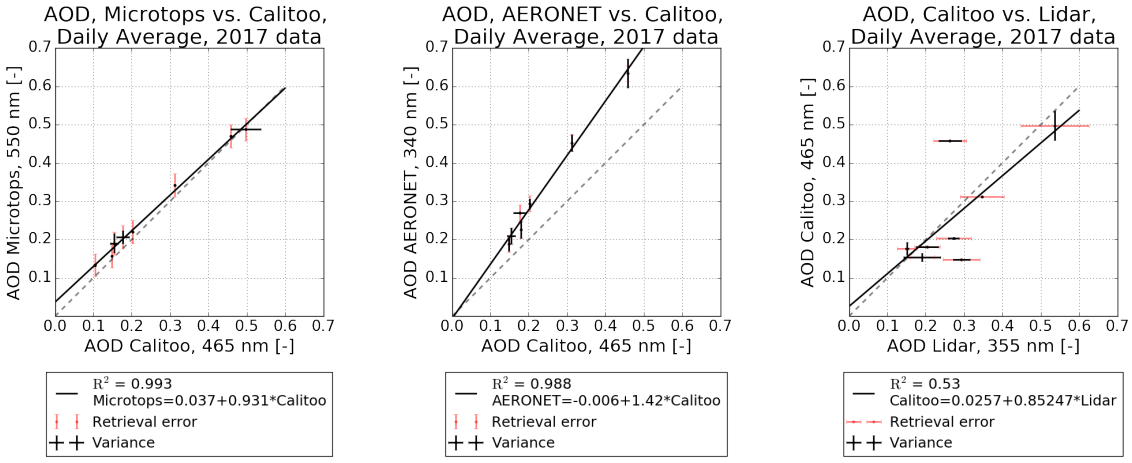

(a) (b) (c)

Figure 4.7: The daily averaged AOD values for the 2017 measurement period retrieved with the lidar, from the Microtops, the Calitoo and AERONET are compared. In (a) the data gathered with the Microtops is compared to the Calitoo, in (b) the AERONET data is compared to the Calitoo and in (c) the Calitoo is compared to our lidar retrieved values for the AOD. The black error bars show the variation around the calculated mean value per day. The red error bars show the retrieval error, 0.03 for the Microtops, 0.021 for the AERONET data, 11 % for the lidar data in 2016 and 16.5 % for the lidar data in 2017. For the Calitoo no retrieval error is indicated.

Different days are taken into account for the Calitoo-Lidar intercomparison than for the Calitoo-AERONET intercomparison, because only the days where both instruments gathered data for the AOD are included, for both intercomparisons separated. That is why it happens that the AERONET data correlates well with the Calitoo data and the Calitoo correlates well with the lidar data, but according to figure 4.6(b) the lidar data does not correlate well with the AERONET data. More days are included in the intercomparison shown in figure 4.6(b).

Because the statistical analysis is done with daily averaged values, it is not a robust correlation study. To look into some details, I point out one striking case. In figure 4.6(b) one of the three data-points is notable because of its low value for the lidar retrieved daily averaged AOD and its quite large value for the daily averaged value for the AOD from AERONET (at $\sim$ 0.07,0.4). We see no variation in the data-point, the averaged values come from only one AOD retrieval from the lidar and one AOD measurement from AERONET in that day, the 23th of August 2017. The AERONET measurement is from 13:01, the lidar selection is from 15:42 to 16:00.

In the figure below the quicklook of the raw data is shown for the 23th of August 2017. The moment of the AERONET measurement is indicated in figure 4.8, although this measurement is not done at this location, this is just to point out the time-difference of the two measurements. The clear-sky selection for the AOD retrieval with the lidar data is shown with the black vertical lines in figure 4.8. A Total Sky Image, shown in figure 4.9(b), is shown for the moment of the lidar retrieval, but from the main ARM site.

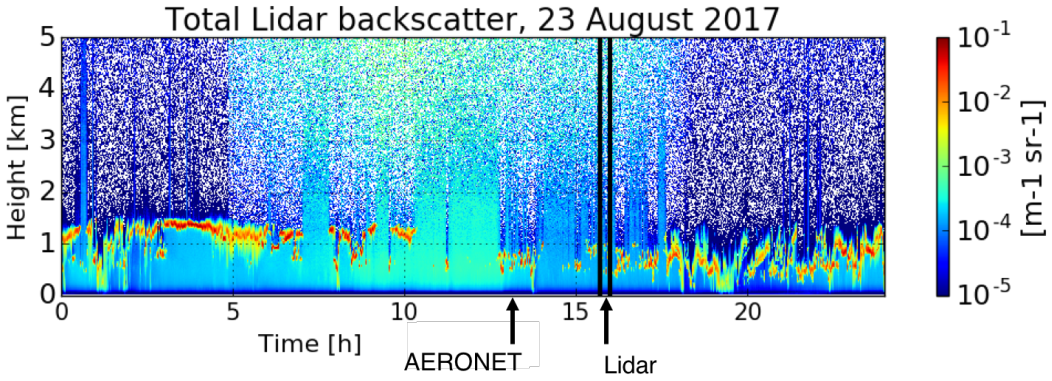

Figure 4.8: The total lidar backscatter in the lower troposphere (0-5 km), for the 23th of August 2017. Where the AERONET arrow is, is the time at which the AERONET AOD is measured, from the main ARM site, 5 km to the east. So this indication is just to point out the time difference. The selection for the lidar AOD retrieval is shown with the arrow and the black vertical lines.

As we see from figure 4.8, clouds are present and visible above the airport site at the moment of the AERONET measurement and as we see from figure 4.9(b) clouds

were present above the main ARM site, where the AERONET sun-photometer was positioned at the moment of the lidar retrieval. From these figures it can clearly be seen that not the same moments for both locations, for the lidar and the AERONET sun-photometer, can be used for the AOD retrievals, as clear-sky periods need to be selected. Therefore averaging over the days or parts of the days is necessary to intercompare.

The AERONET measurement is from 13:01 and has a value of 0.397. With our method we did not retrieve an AOD value for this moment, because clouds were present above the lidar. The averaged ATB for the lidar retrieval is shown in figure 4.9(a). The integrated aerosol extinction coefficient, the AOD is 0.07, with the standard value of the normalisation height of 7000 m. Which is highly unlikely the true value. If we change the normalisation height to 6500 m, the output from the Klett inversion method for the AOD is 0.31, which deviates a lot from the value found with the standard used normalisation height of 7000 m, and compared to the average AOD value in the 2017 measurement period is a better estimation of the true value. So again, the uncertainty by the estimation of the normalisation height is large and highly important for the intercomparisons.

Also at the moment of our retrieval, from 15:42 until 16:00, a low-level thin cloud was present above our lidar, which we see from the little bump around 750 m in the averaged ATB profle, figure 4.9(a). So the retrievals for this day are highly uncertain because of the presence of clouds and the large uncertainty in the lidar AOD retrieval due to the estimation of the normalisation height.

When instead of all the daily averages, only the measurements that are within an hour from each other from the AERONET data and the lidar selections are used, the correlation coefficient turned out to be 0.003, significantly smaller than the correlation coefficient when all the daily averages were taken into account. Only 5 lidar measurements were taken into account in this analysis. Because of this small amount of data-points, an incorrect lidar retrieval has a large effect at the correlation analysis. Unfortunately no more measurements from AERONET and the lidar were gathered within an hour from each other. So reducing the time-intervals for averaging does not increase the correlation of the lidar AOD retrievals with the AERONET data.

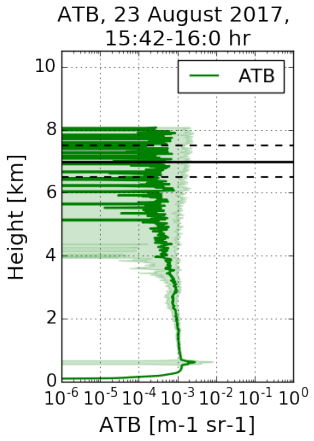

(a)

(b)

Figure 4.9: In (a) the averaged ATB for one selection on the 23th of August 2017 is shown, the selection is shown with the black lines in figure 4.8. The shading is the standard deviation. The black line shows $z_0 = 7000$ m, the standard value. The dashed lines show $z_0 = 6500$ m and $z_0 = 7500$ m. In (b) a Total Sky Image is shown from 15:50, so during the lidar selection but taken at the main ARM site, 5 km to the east. Clouds were present above the main ARM site while a clear-sky selection is made for that moment above the lidar.

4.2.4. Aerosol vertical distribution 2017

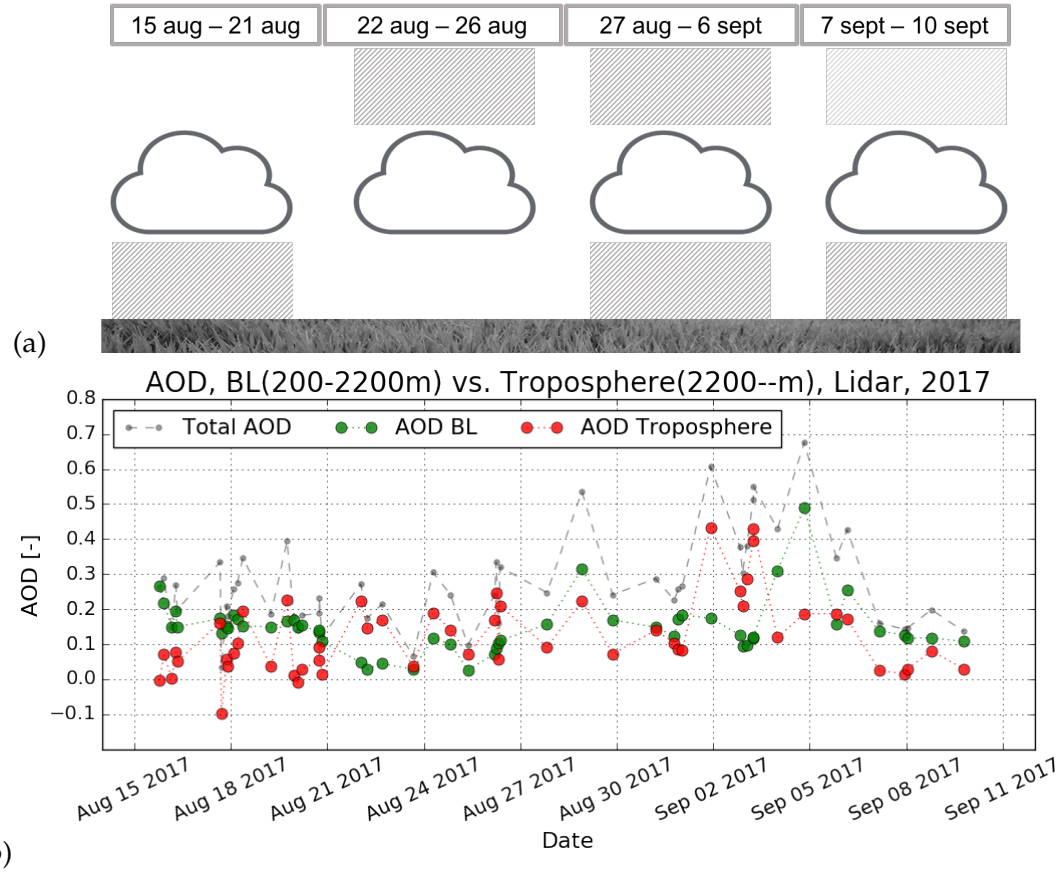

Figure 4.10: The subdivision of the measurement period in 2017 regarding the aerosol vertical distribution is shown in (a). The CLARIFY scientist made this subdivision after analyzing the preliminary results for aerosol number density concentrations, scattering coefficients and the data gathered with mass spectrometers. The gray diagonal stripes indicate smoke/dust aerosols. Thicker stripes for more aerosol. In (b) the AODs for the clear sky selections in the 2017 measurement period are shown. The total AOD, the same as in figure 4.3(a), is shown in gray. The integrated aerosol extinction in the BL is shown in green and the integrated aerosol extinction in the troposphere is shown in red.

In addition to the calculation of the AOD, the vertical distribution of the aerosols can be analyzed from the lidar signal. The results are shown below, in comparison with a subdivision of regimes for the measurement period in 2017, regarding the vertical distribution of the aerosols, made by CLARIFY scientists. Aerosols in the form of smoke or dust were always present during the period in 2017, the altitude at which they were present varied during the period. The CLARIFY team made a subdivision of the measurement period in 2017 ('personal communication, 2017'),

regarding where the smoke was present based on in situ data and model data, in the boundary layer, above, both or non. This subdivision is visualized in figure 4.10(a).

With the lidar retrievals, we tried to see if we could study the same thing, the vertical distribution of the aerosols. To check whether the aerosols detected are present in the boundary layer (BL), or above, in the free troposphere, the aerosol extinction coefficient is integrated separately for the two layers (from 200 to 2200 m for the boundary layer and from 2200 to 8000 m for the free troposphere). The results are shown in figure 4.10(b).

A trend can be seen in figure 4.10(b). The AOD in the BL is at the start of the period larger than the free tropospheric AOD. From 21 Augustus onward a clear shift is visible in the lidar results for the AOD, the free tropospheric AOD is larger than the BL AOD. From 27 Augustus until the end of the period the total AOD, shown with the gray dots in figure 4.10(b) is larger than in the first half of the period, and in the end the BL AOD is larger than the free tropospheric AOD, which again corresponds to the division of the regimes, as was visualized in figure 4.10(a). The vertical distribution can be analyzed from the lidar retrieved aerosol extinction profiles.

To study the causes for the aerosols to be in the boundary layer or in the upper atmosphere, two cases are studied in further detail. One selection, on the 16th of August 2017, in the first regime, where aerosols were mostly present in the lower atmosphere, the boundary layer. And one selection, on the 24th of August 2017, in the second regime, where aerosols were mostly present in the upper atmosphere, the free troposphere. Both selections are around 7 AM. The raw data for the total lidar backscatter and the lidar depolarisation ratio for both selections is shown in figures 4.11(a,b,d,e).

In figure 4.11 we see that the total lidar backscatter and the lidar depolarisation ratio for the selection on the 16th of August are relatively larger in the boundary layer compared to the total lidar backscatter and the lidar depolarisation ratio for the selection on the 24th of August. In this selection on the 24th of August, the boundary layer is clean, and the aerosols are higher up in the atmosphere, in the free troposphere. This vertical distribution can also be seen in the aerosol extinction profiles shown in figures 4.11(c,f), calculated from the Klett inversion method. The profile for the 24th of August has larger values for the aerosol extinction up to 5 km, where the values for the aerosol extinction on the 16th of August are significantly smaller from 2 km in altitude upwards. The AOD calculated from the integration of these profiles are 0.269 for the selection on the 16th of August and 0.304 for the selection on the 24th of August. So the aerosol extinction has overall larger values for the selection on the 24th of August.

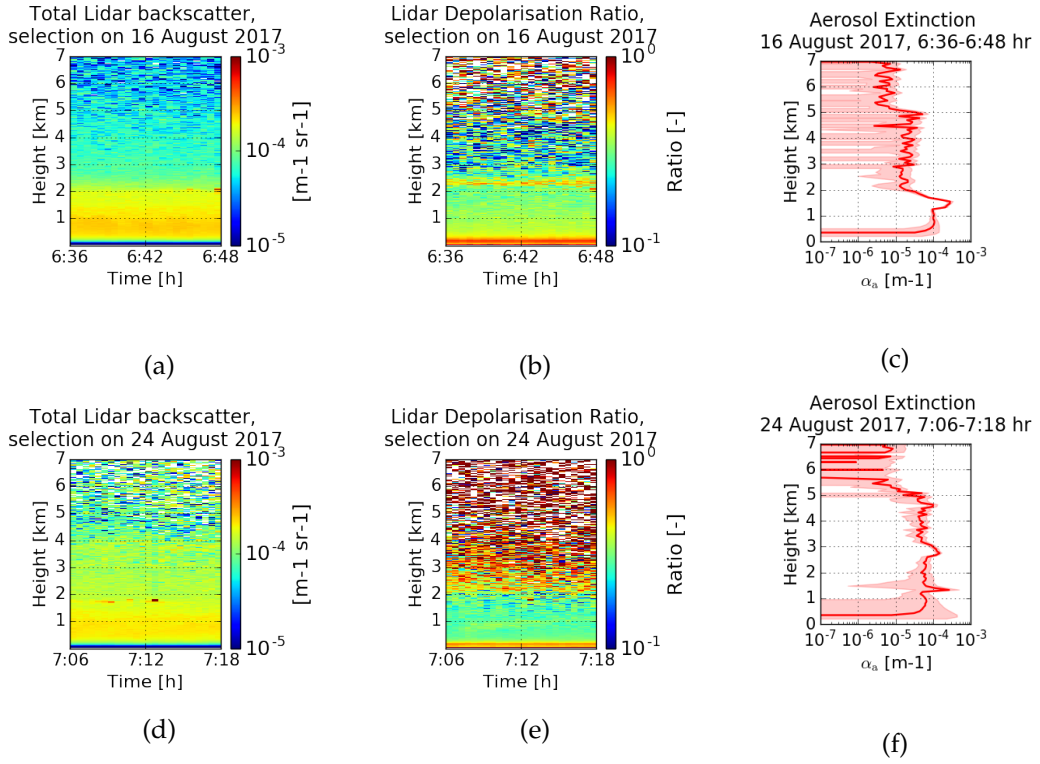

Figure 4.11: The total lidar backscatter, lidar depolarisation ratio and averaged aerosol extinction profiles for two selections, one on the 16th and one on the 24th of August 2017. In (a) and (d) the total lidar backscatter in the lower troposphere (0-5km) for a selection on the 16th (a) and the 24th (d) of August is shown. In (b) and (e) the lidar depolarisation ratio in the lower troposphere for the two selections is shown. In (c) and (f) the averaged aerosol extinction profiles for the 16th (c) and the 24th (f) of August are shown. The aerosol extinction vertical profile is averaged over the selection in time. And is averaged in the vertical over 5 range gates to smooth the profile.

The difference in the aerosol vertical distribution is caused by for example, a different wind speed, wind direction, temperature vertical profile, humidity or a different source of the aerosols (Szabó-Takács, 2011). We studied a few of these effects for the two selections as were given above, for the 16th of August 2017 and the 24th of August 2017. For the wind, temperature and humidity data, general meteorological data measured at the surface from the main ARM site is used.

In the measured relative humidity at ground-level a significant difference is found between the two selections. 76 % on average for the selection on the 16th of August and 95 % on average for the selection on the 24th of August. This high relative humidity for the selection on the 24th of August can cause the aerosols to be high in extinction and therefore cause the larger value for the total AOD (Xu et al., 2015). We know from observations and the notes we kept up during the measure-

ment period that in the second regime, 22th until the 26th of August, more precipitation events happened than in the first week of the 2017 measurement period. This could have influenced the relative cleaner boundary layer in the second regime.

Also, another wind speed and direction are measured at the surface during the two different selections. 6.3 m/s from the EESE for the selection on the 16th of August and 5.7 m/s from the SE for the selection on the 24th of August. This means that the air we measured on the 16th of August has blown over the island east to west before we detected the vertical profile with the lidar at the airport site. For the selection on the 24th of August we measured air that came straight from the ocean blowing over the island from the SE. To be able to say something about the vertical distribution, the type of aerosol and to link this to the dynamical processes, the sources of the aerosol should be tracked-back.

The type of aerosol affects the amount of depolarisation the lidar will measure, as described in the previous chapter. Spherical particles will cause the lidar to detect backscattered light pulses with a parallel plane of polarization in reference to the emitted light pulses, while non-spherical particles will depolarize the light. Dust and smoke are typically non-spherical particles and will therefore depolarize the light. To study which aerosols we detected at what altitude during these two cases, HYSPLIT back-trajectories are made using the NOAA HYSPLIT Trajectory Model (Stein et al., 2015). For three altitude levels, the air is tracked back for 10 days, 240 hours. In figure 4.12(a) the back-trajectory ending on the 16th of August 7 AM is shown. On the 16th of August we detected non-spherical particles in the boundary layer as the depolarisation ratio is larger than zero. From the back-trajectories we learn that the air in the boundary layer on Ascension Island at the 16th of August 7 AM, is originating from above western Africa, which indeed means biomass burning aerosol could be in the air. In figure 4.12(b) we see that the air reaching Ascension Island on the 24th of August 7 AM, in the boundary layer, is coming more from the south and has blown for at least the last five days through the boundary layer over the Atlantic ocean, which means that the air is clean of biomass burning smoke or dust, because less biomass burning events happen in the south of Africa and due to turbulent mixing and precipitation events that clean the boundary layer. The air above, at 2000 m and 4000 m in altitude for this selection, does originate from western Africa, which means that the chance is large that dust or biomass burning aerosol is present in this air, which causes the larger depolarisation ratios measured in the altitude domain 2000 m-5000 m for the selection on the 24th of August compared to the case on the 16th of August. This second case, on the 24th of August, is a typical situation where thus the boundary layer air is clean of smoke and dust, only contains marine aerosol and the layers above do contain smoke from the biomass burning events in Africa or Saharan dust. To really define the cause in the difference in vertical distribution, further research needs to be done, especially by taking into account the characteristics of the aerosols and the dynamical processes.

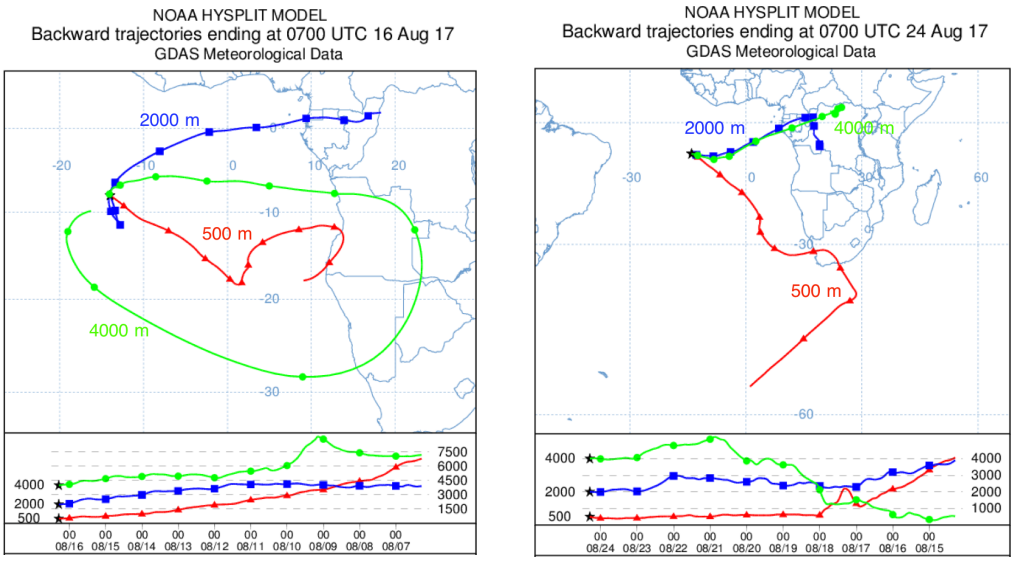

(a) (b)

Figure 4.12: HYSPLIT Backtrajectories for two selections in 2017, for 240 hours and 3 altitude levels. In (a) the back-trajectories ending on the 16th of August 2017, 7 AM are shown. In (b) the back-trajectories ending on the 24th of August 2017, 7 AM are shown. With the red line, the air which reaches Ascension Island at 500 m altitude is shown. With the blue line, the air which reaches Ascension Island at 2000 m altitude is shown. With the green line, the air which reaches Ascension Island at 4000 m is shown. In the plots on the bottom of the figures, the altitude of the parcels reaching Ascension Island at the specific altitudes, is shown over the days. With on the left the moment we are interested in and to the right the ten days the parcel has travelled.

4.3. Cloud parameters

For both measurement periods, in 2016 and 2017, the cloud parameter R_{eff}^{100} is calculated from the lidar data with the MS based inversion method and compared to R_{eff}^{100} retrieved from the radar data with Frisch's methods. But first the reference height in the cloud of 100 m abouve cloud base height is validated, whether the same is used in both methods. For the lidar retrievals, the cloud selections were made by a visual inspection of the raw data, the total lidar backscatter, selecting homogeneous stratocumulus clouds with a thickness of at least 100 m and a cloud base height of at least 1000 m. These selections were used to calculate the effective radius and cloud extinction profiles, with the MS based inversion method. From this, we use the effective radius at the reference height in the cloud to compare our retrievals with the ones we retrieved from the ARM Cloud Radars. The effective radius at 100 m above cloud base height, retrieved from the lidar data with the MS based inversion method, is shown for both periods in figure 4.16(a) and 4.17 (a).

Importance of the Cloud Base Height

For the cloud parameter retrieval a reference height of 100 m above cloud base height (CBH) is used. It is of big importance that the parameters with which we want to compare our results with are the parameters at this same relative height in the cloud, as the effective radius has a large dependency on the height in the cloud (Zhang et al., 2011). The CBH in the lidar retrievals is a product of the MS based inversion method and not a real direct measured quantity, as described in the previous chapter. This produced CBH from the lidar retrieval needs to agree with the CBH used in the radar method, to make sure the same reference height above these CBHs is used for the R_{eff}^{100} intercomparison. The radar data is gathered from the main ARM site, therefore the CBH can not be compared directly with the one we retrieved from the lidar data, at the airport site, because they are at 5 km spatial distance from each other. For the CBH in the radar retrieval method, at the ARM site, we used the CBH

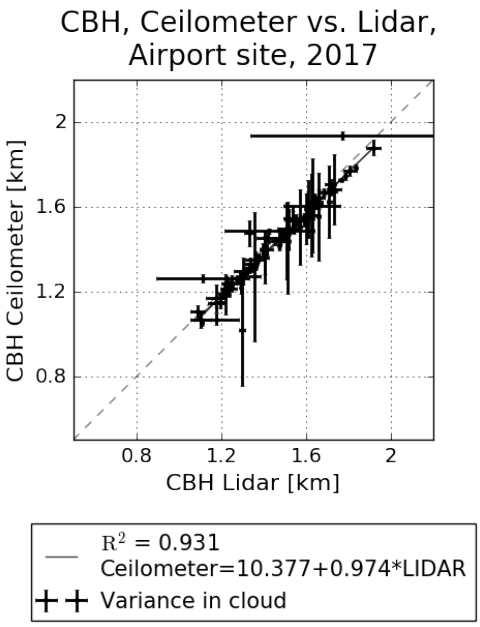

Figure 4.13: The CBH for the cloud selections in the 2017 measurement period, retrieved with the ARM Ceilometer and the lidar, both at the airport site. With the error bars the standard deviation in the cloud, the variation around the mean is shown.

measured by a Ceilometer. An identical instrument is operated by the ARM at the airport site, so the CBH we retrieved from the lidar data for the cloud selections, is compared to the CBH measured by the Ceilometer at the airport site at those moments, shown in figure 4.13 and 4.14. This CBH from both instruments is corrected for the altitude above mean sea level of the instrument so the CBHs in the figures are the CBHs above mean sea level. Assuming that the Ceilometer at the airport site and the Ceilometer at the ARM site are similar, we can conclude that the CBH we use in the lidar retrieval and in the radar retrieval are similar and thus the reference height in the cloud correspond well and the intercomparison of the parameters at this reference height can be done.

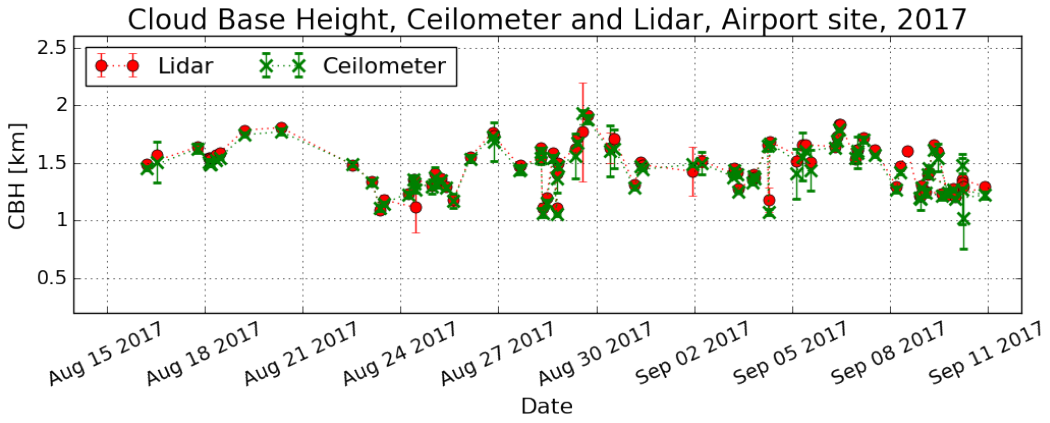

Figure 4.14: The CBH both measured with the lidar and the ARM Ceilometer at the airport site, for the R_{eff}^{100} retrieval selections. With the red dots the CBH retrieved from the lidar data, from the aiport site, is shown. With the green crosses the CBH detected by the Ceilometer operated by the ARM at the airport site, for the same time-selections, is shown. With the error bars, the standard deviation in the cloud, the variation around the mean is shown.

However, a new study, performed by Y. Blanchard ('personal communication, 2018'), during our 2017 measurement period, has shown that there is a higher cloud fraction above the main ARM site than above the airport site. So not all CBHs and cloud fraction are similar above the airport site and the main ARM site. To show this, the CBHs measured by the Ceilometer at the airport site and the CBH measured by the Ceilometer at the main ARM site are shown in figure 4.15 for one day, the 26th of August 2017. Again, the CBH is corrected for the altitude above mean sea level of the instrument, so the CBHs are given in altitude above mean sea level. As can be seen, more low-level clouds are detected above the main ARM site. So overall the cloud fraction and CBH can not be assumed to be similar over the airport site and main ARM site. Because the main difference is in the low-level clouds, with a CBH below 1000 m in height, this does not affect our intercomparison, be-

cause for our retrievals we select clouds on the constraint that the CBH is at least 1000 m.

So for the intercomparison of R_{eff}^{100}, we conclude from figure 4.13 that the reference height in the cloud 100 m above the CBH can be used to compare the R_{eff} but we do need to take into account for further analysis that the cloud characteristics can be different at the different locations.

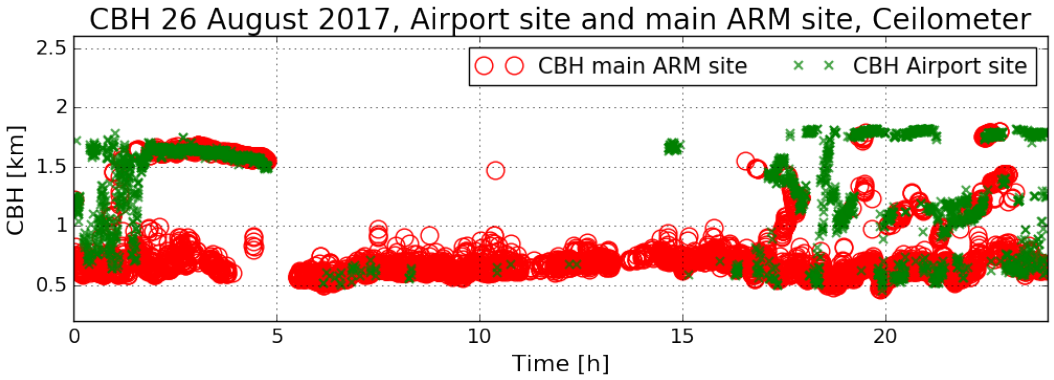

Figure 4.15: The CBH from the Ceilometer at the Airport site compared to the CBH from the Ceilometer at the main ARM site for one day, the 26th of August 2017. With the red circles the CBH detected above the main ARM site is shown. With the green crosses the CBH detected above the airport site is shown. Both are measured with similar Ceilometers operated by the ARM.

4.3.1. Cloud parameters retrieval from lidar data

The uncertainties in the retrieval for the cloud parameters with the lidar data and the MS based inversion method arise from the estimation of the instrument calibration coefficients, the measurement errors and the uncertainty in the method. A priori estimates are assigned to the calibration coefficients, as was described earlier. The uncertainties in the calibration coefficients and the uncertainties in the MS based inversion method together give the retrieval error, 19.8 % on average for 2016 and 39.1 % on average for 2017. This retrieval error is significantly larger in 2017 due to the large uncertainties in the estimation of the calibration coefficients, for the misalignment. The results for the retrieval of R_{eff}^{100}, from the MS based inversion method, for both measurement periods are shown in figures 4.16(a) and 4.17(a). The black error bars show the variation around the mean value for a cloud selection, the standard deviation. The retrieval error is shown with the gray shading.

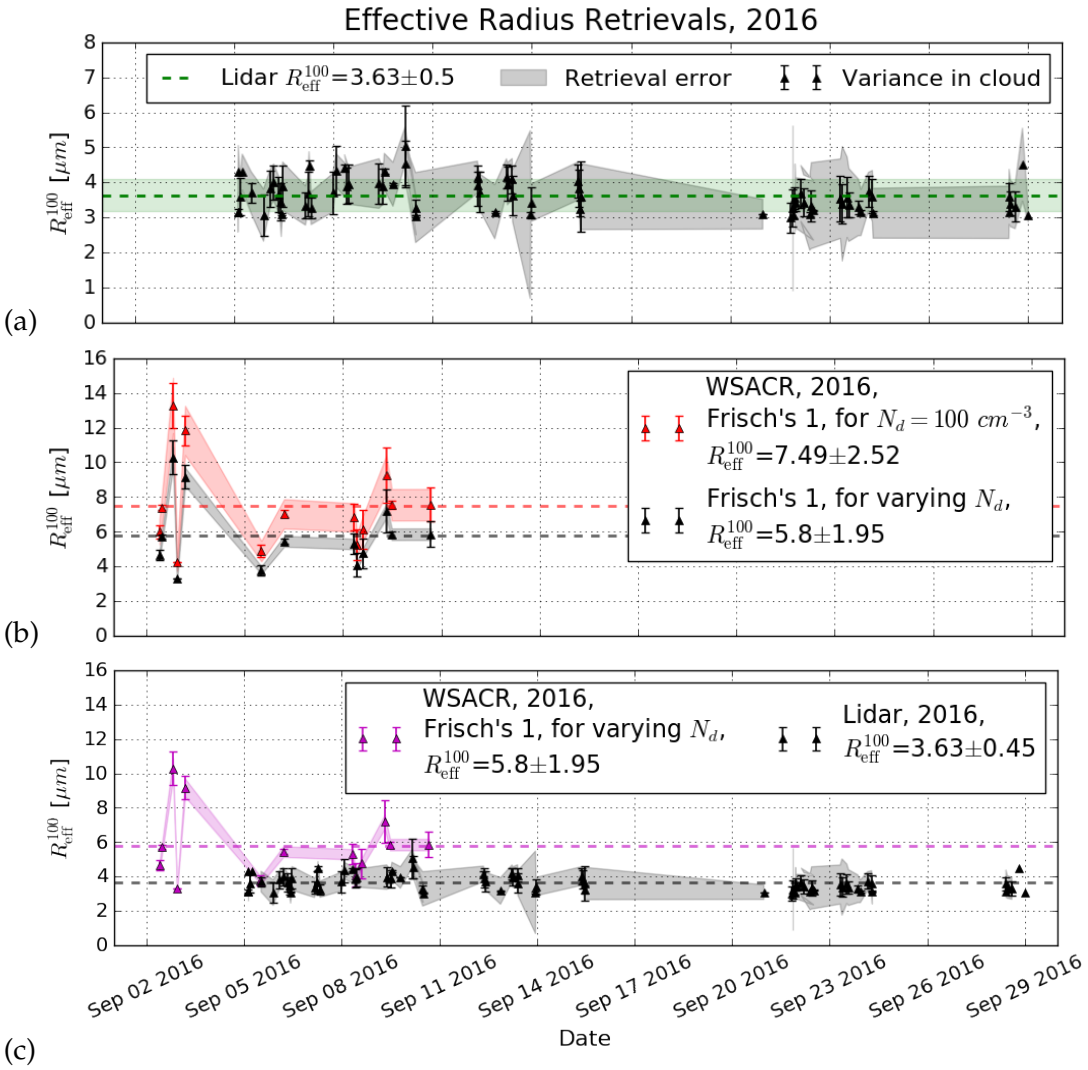

Figure 4.16: In (a) the lidar retrieved R_{eff}^{100} for the clouds selected in the 2016 measurement period is shown. The y-axis has another range than in (b) and (c). The error bars show the standard deviation in the cloud. The shaded area shows the retrieval error, 19.8 %. The mean R_{eff}^{100} during the 2016 measurement period is shown by the green dashed line, the shading around this dashed line is the standard deviation. In (b) the R_{eff}^{100} results are shown for the radar retrievals, for $N_d = 100\ \text{cm}^{-3}$ in red and for the variable daily averages retrieved from the lidar as input for N_d in black. $\sigma_x = 0.34$ in both retrievals. The error bars show the standard deviation in the cloud. The shaded areas show the retrieval errors, 12 % when $N_d = 100\ \text{cm}^{-3}$ and 5.7 % for the variable daily averages as input for N_d. The mean R_{eff}^{100} during the 2016 measurement period is shown by the dashed lines and in the legend. In (c) the R_{eff}^{100} results retrieved with the lidar and with the radar are shown, for the variable daily averages as input for N_d and with $\sigma_x = 0.34$. The error bars show the standard deviation in the cloud. The shaded areas show the retrieval errors, 5.7 % for the radar retrieval and 19.8 % on average for the lidar retrieval. The mean R_{eff}^{100} for the radar and the lidar retrievals, during the 2016 measurement period, are shown by the dashed lines and in the legend.

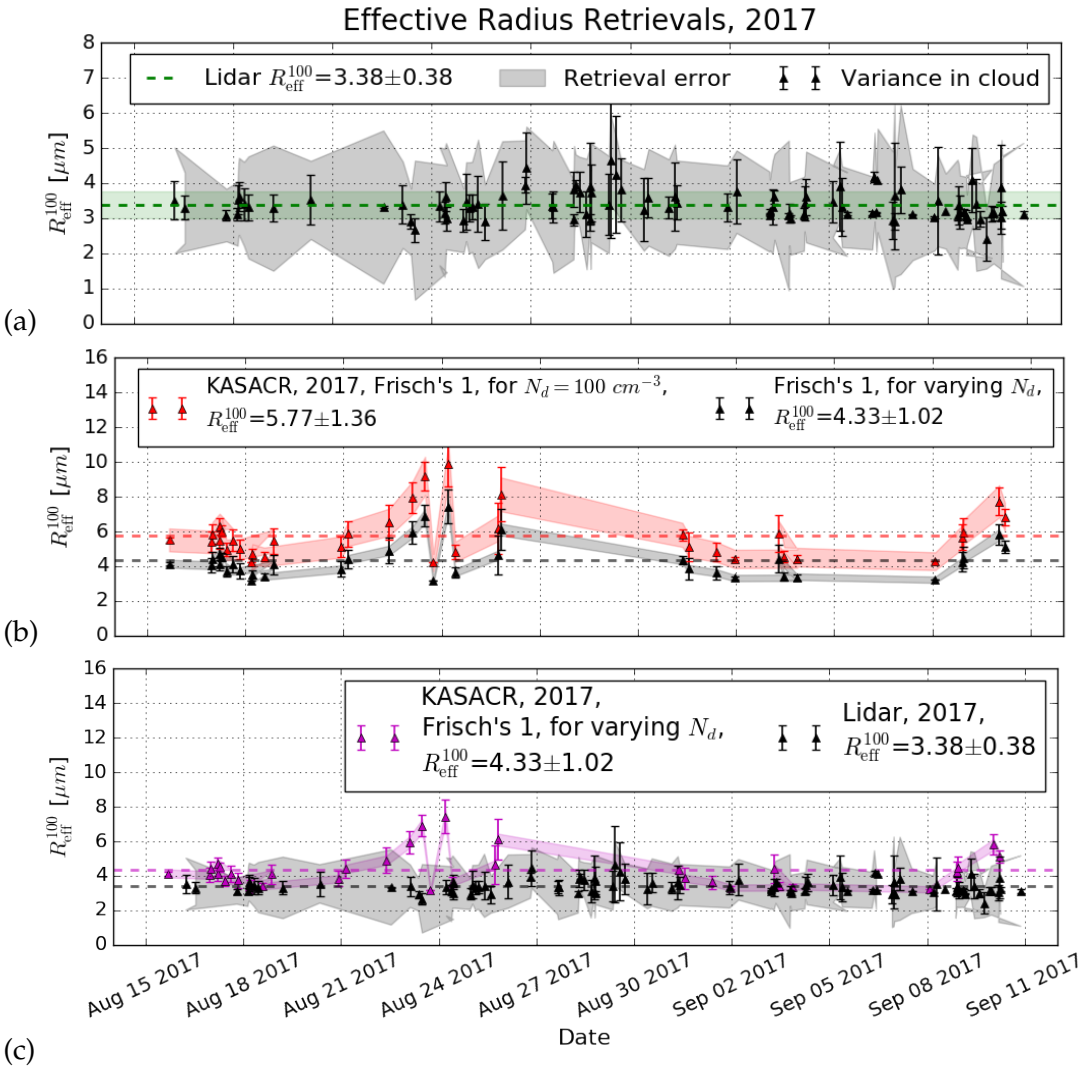

Figure 4.17: In (a) the lidar retrieved R_{eff}^{100} for the clouds selected in the 2017 measurement period is shown. The y-axis has another range than in (b) and (c). The error bars show the standard deviation in the cloud. The shaded area shows the retrieval error, 39.1 %. The mean R_{eff}^{100} during the 2017 measurement period is shown by the green dashed line, the shading around this dashed line is the standard deviation. In (b) the R_{eff}^{100} results are shown for the radar retrievals, for $N_d = 100\ \text{cm}^{-3}$ in red and for the variable daily averages retrieved from the lidar as input for N_d in black. $\sigma_x = 0.34$ in both retrievals. The error bars show the standard deviation in the cloud. The shaded areas show the retrieval errors, 12 % when $N_d = 100\ \text{cm}^{-3}$ and 5.6 % for the variable daily averages as input for N_d. The mean R_{eff}^{100} during the 2017 measurement period is shown by the dashed lines and in the legend. In (c) the R_{eff}^{100} results retrieved with the lidar and with the radar are shown, for the variable daily averages as input for N_d and with $\sigma_x = 0.34$. The error bars show the standard deviation in the cloud. The shaded areas show the retrieval errors, 5.6 % for the radar retrieval and 39.1 % on average for the lidar retrieval. The mean R_{eff}^{100} for the radar and the lidar retrievals, during the 2017 measurement period, are shown by the dashed lines and in the legend.

4.3.2. Cloud parameters intercomparison

Frisch's method 1 is applied to selections from the Cloud Radar data for the 2016 and 2017 measurement periods, the results are shown in figure 4.16 (b) and 4.17 (b), both for the standard value of 100 cm^{-3} for the N_d and for the daily averaged N_d values from the lidar retrieval as input for the a-priori defined N_d.

The uncertainties from the method are calculated, first for the 2016 data. We used $\sigma_x = 0.34 \pm 0.09$, $N_d = 100 \pm 70$ cm^{-3} and $N_d = 466.1 \pm 127$ cm^{-3} for the standard value of 100 cm^{-3} and the variable daily averages as input respectively, and an expected uncertainty in the measurement of ± 3 dBZ in the reflectivity factor. In 2017 $N_d = 540.4 \pm 142$ cm^{-3} is used for the variable daily averages as input, for the other parameters the same values as in 2016 are used. The error for the R_{eff} retrieval, for method 1, is calculated to be 12 % in 2016 and 2017 for the standard value of $N_d = 100$ cm^{-3} as input. 5.7 % in 2016 and 5.6 % in 2017 for the variable daily averages as input for N_d.

Dependency on Droplet Size Distribution in Radar Method

The lognormal cloud droplet size distribution used in the radar method, was described in equation 3.7. The effect of the pre-defined estimation for the lognormal cloud droplet spread on the cloud droplet size distribution and therefore the retrieved R_{eff}^{100} is studied here.

This dependency on σ_x is studied only for the 2017 measurement period. For N_d the average cloud droplet number concentration as retrieved from the lidar for 2017 was used, 540.4 cm^{-3}. R_0 is the median radius, we used the average R_{eff}^{100} retrieved from the radar with Frisch's method 1 for 2017, 4.33 µm. To define the possible bias error from the uncertainty in σ_x, the values for σ_x were varied and the R_{eff}^{100} for the cloud selections and the average were calculated. The values for σ_x used in the evaluation are 0.1, 0.2, 0.3, 0.4, 0.5 and 0.6. The resulting droplet size distributions are shown in figure 4.18. The retrieval errors change slightly from a change in σ_x. The uncertainty in Frisch's method 1 with $N_d = 540.4 \pm 142$ cm^{-3} and $Z = -30 \pm 3$ decibel, is 4.8 % for $\sigma_x = 0.1 \pm 0.09$ and 7.1 % for $\sigma_x = 0.6 \pm 0.09$. The average value for R_{eff}^{100} in 2017 calculated for the standard value for σ_x, 0.34, and with the varying value for N_d with the calculated daily average N_d from the lidar as input, was 4.33±1.01 µm as we saw in figure 4.17(b). The average value for R_{eff}^{100}

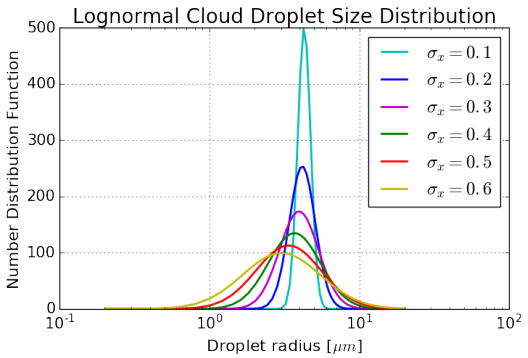

Figure 4.18: The cloud droplet size distributions for the radar method, with $N_d = 540.4\,\mathrm{cm}^{-3}$, $R_0 = 4.33$ µm and for varying values of the lognormal spread, σ_x.

is 4.57±1.06 µm for $\sigma_x = 0.1$ and 3.83±0.89 µm for $\sigma_x = 0.6$. The change in R_{eff}^{100} resulting from the variation in σ_x is shown in figure 4.19. The exact averaged values for R_{eff}^{100} over the measurement period are shown in the legend.

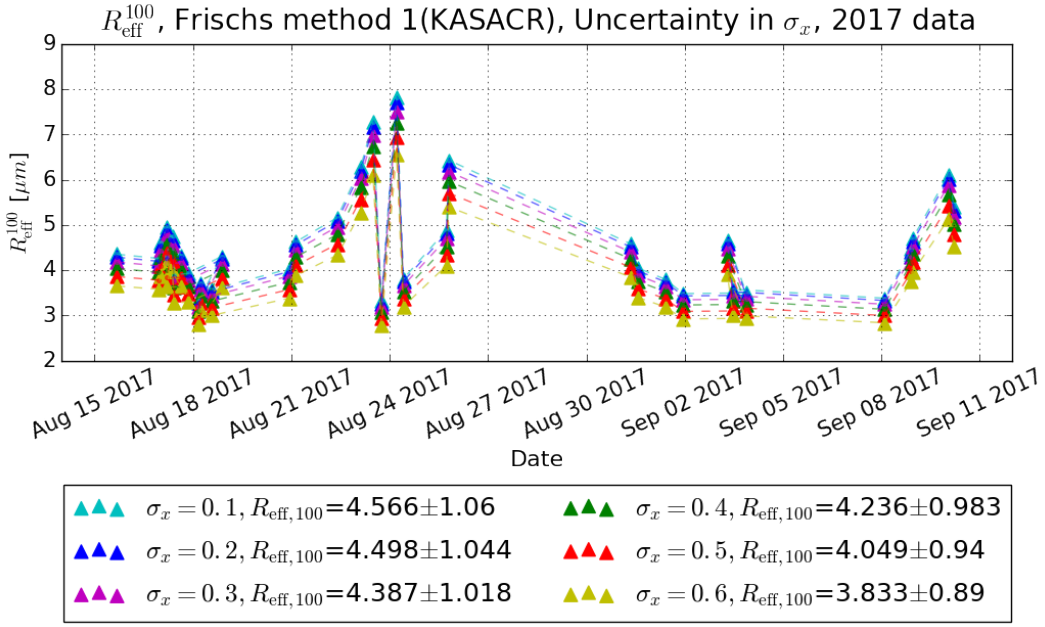

Figure 4.19: R_{eff}^{100} for the clouds selected in the 2017 measurement period, retrieved with Frisch's method 1 with the variable daily averages as input for N_d. Shown for varying values of the assumed lognormal spread of the cloud droplet size distribution.

The retrieved R_{eff}^{100} from the lidar is compared to the retrieved R_{eff}^{100} with Frisch's method 1 from the radar data. The results are shown in figure 4.16 (c) and 4.17 (c). The shaded areas in the figures are the retrieval errors, the error bars visualize the standard deviations in the cloud.

It is difficult to say something about the intercomparison in 2016 because the WSACR was only operating for 9 days during our measurement period which resulted in 13 useful cloud selections. In 2017 the KASACR was working for the full measurement period, which resulted in 36 useful cloud selections. In 2017 we can see that the lidar retrieved R_{eff}^{100} corresponds with the radar retrieved R_{eff}^{100} within the uncertainty band. Around the 23th/24th of August in 2017, the radar results show significantly higher values than average, this is due to drizzle. The radar method is highly sensitive to the presence of drizzle (Frisch, Fairall et al., 1995) because the reflectivity is proportional to the diameter of the droplet to the sixth power. Filtering for drizzle is done, but as this might have not been done properly, this results in significantly larger values for the retrieval of R_{eff}^{100} for rainy periods, where drizzle-free selections were difficult to define. Cloudnet data, for example, is

filtered for drizzle (Illingworth et al., 2007), using this might improve the retrieval.

Taking into account the uncertainty in the radar retrievals due to the large sensitivity to drizzle, the measurement errors and the uncertainty in the method, and the uncertainties in the lidar retrievals due to the estimation of the calibration coefficients, the measurement errors and the uncertainties in the method, the results for the R_{eff}^{100} from the lidar retrievals and the radar retrievals show a significant correlation for the 2017 measurement period. Therefore the retrieval of the R_{eff}^{100} from the lidar data with the MS based inversion method seems promising.

Frisch's Method 2

In addition to the method described above, Frisch's method 1, also Frisch's method 2 is used to calculate the R_{eff}^{100} in the 2016 measurement period. This method uses measurements for the LWP by the MWR. No assumption for N_d is needed now. The used LWP data points for Frisch's method 2 for 2016 are shown in figure 4.21(b). The uncertainties in Frisch's method 2 are dependent on the errors in Z and σ_x, and the instrument error for the LWP. With the same values for Z and σ_x as was used for method 1, and with an assumed error in the LWP measurement of 20 %, the error in method 2 for the 2016 data is calculated to be 14 %. The results for the R_{eff}^{100} retrieved with Frisch's method 2 for 2016 are shown in figure 4.21(c). As the results have large uncertainties and because we have only 7 data points in 2016, the data is not used for the intercomparison with the lidar retrievals. We only looked at the methods in comparison to each other. The results differ a lot when we look at the retrievals from Frisch's method 1 and Frisch's method 2, the intercomparison is shown in figure 4.20.

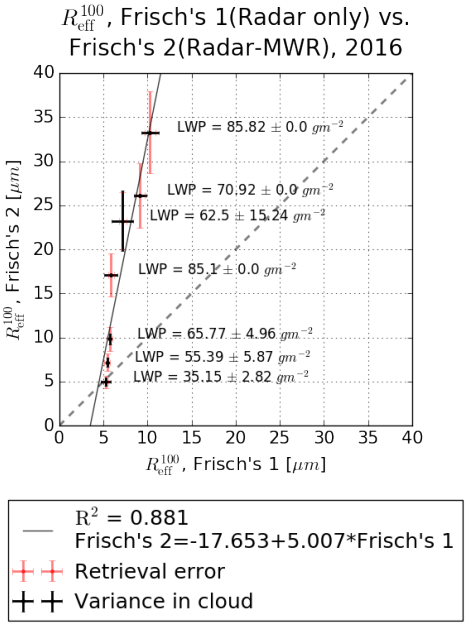

Figure 4.20: R_{eff}^{100} for the clouds selected in the 2016 measurement period and retrieved with Frisch's method 1 and method 2. The black error bars show the standard deviation in the cloud, the variation around the mean. The red error bars show the retrieval error, 5.7 % for method 1 and 14 % for method 2.

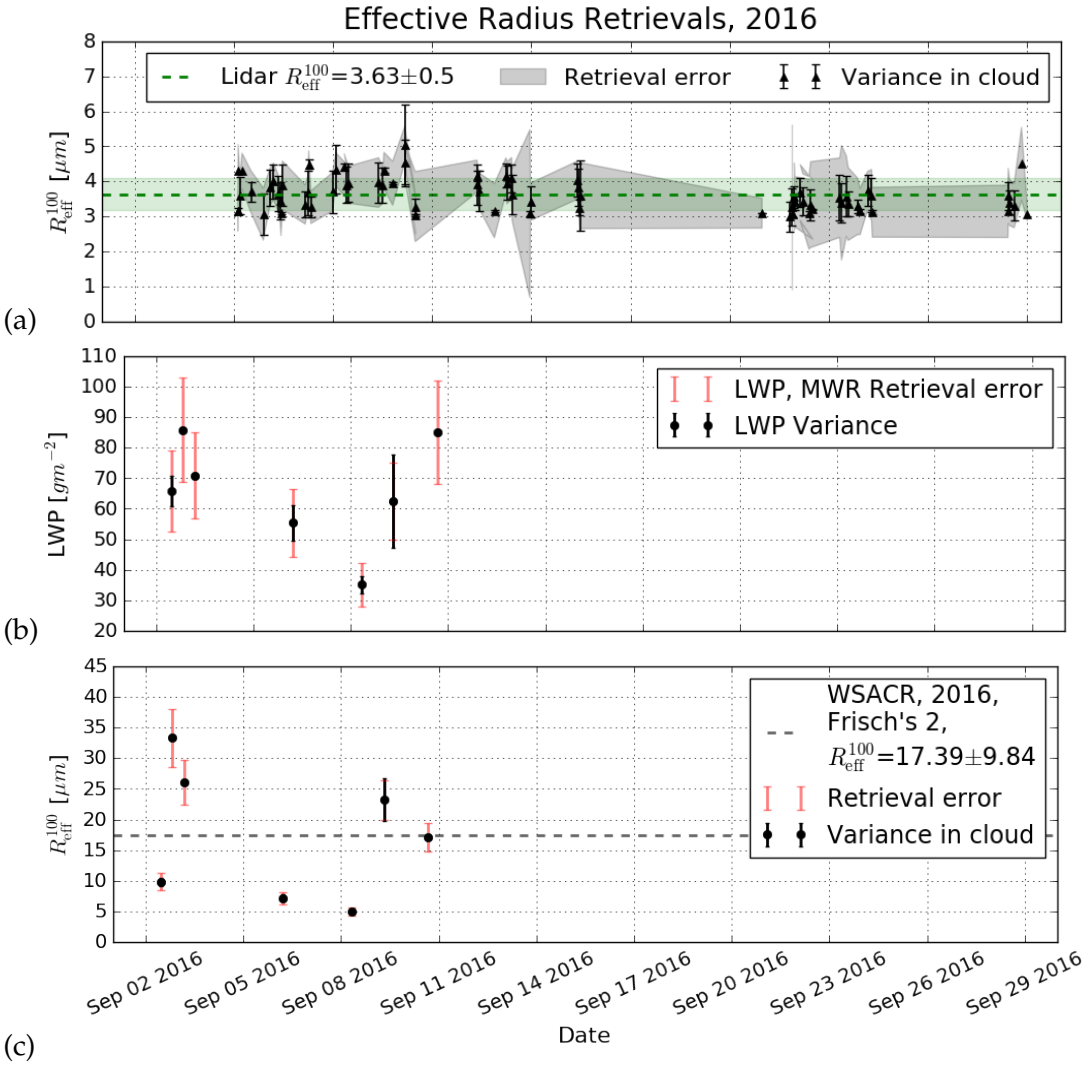

Figure 4.21: In (a) the lidar retrieved R_{eff}^{100} for the clouds selected in the 2016 measurement period is shown. The y-axis has another range than in (c). The error bars show the standard deviation in the cloud. The shaded area shows the retrieval error, 19.8 %. The mean R_{eff}^{100} during the 2016 measurement period is shown by the green dashed line, the shading around this dashed line is the standard deviation. In (b) the LWP from the MWR during the cloud selections in the 2016 measurement period is shown, averaged per cloud selection. The black error bars show the standard deviation in the cloud. The red error bars show the 20 % error in the measurement of the LWP. In (c) the R_{eff}^{100} at reference height for the clouds selected in the 2016 measurement period, retrieved with Frisch's method 2 are shown, for $\sigma_x = 0.34$. The y-axis has another range than in (a). The black error bars show the standard deviation in the cloud. The red error bars show the 14 % uncertainty. The mean R_{eff}^{100} retrieved with Frisch's method 2 during the 2016 measurement period is shown in (c) by the gray dashed line and in the legend.

4.4. Deriving Aerosol-Cloud Interactions

For both measurement periods the daily averages for the cloud droplet number concentration and the effective radius at reference height are calculated and plotted against the daily averaged AOD. The results are shown in figures 4.22 and 4.23. The retrieval errors are taken into account for the effective radius and shown by the red error bars in 4.22(c) and 4.22(d). For N_d the retrieval errors are not shown, they are significantly smaller than the retrieval errors in R_{eff}^{100} and than the standard deviations for N_d per day. The gray error bars show the standard deviations from the averaging over the day. So on the left, in (a) and (c) the results for the 2016 measurement period are shown, a slight increase of the N_d is observed with an increase of the AOD. And a slight decrease in the R_{eff}^{100} is observed with an increase of the AOD. This is as expected, as written before. The correlation coefficients are small, so no firm conclusions can be made from this analysis, but it looks promising. In 2017 the correlation coefficients are even smaller and these relationships cannot be concluded, because of the low SNR and therefore the large uncertainties. To refine the analysis for the ACIs a classification for the days is defined.

A classification is made for the days per measurement period, to select if the day was a *clean*, *mixed* or *separated* case. In appendix A.3 lists are shown of which days fell into what category for both measurement periods. The classification was made by a visual inspection of the raw data, the total lidar backscatter. A *clean* day was a day without smoke or dust present. A *mixed* day was a day where an aerosol layer was mixed in with the cloud layer. A *separated* day means that an aerosol layer was detected, vertically separated from the cloud layer. A layer of clean air separates the cloud layer and the aerosol layer. Per category, the average R_{eff}^{100} and N_d are calculated and shown in the figures below.

In 2016 the *clean* days have on average a cloud droplet number concentration of 413.7 cm^{-3}, where the *mixed* days have an average of 489.9 cm^{-3} for N_d. The averaged R_{eff}^{100} is 3.9 µm for *clean* days and 3.5 µm for *mixed* days in 2016. An increase of N_d and decrease of R_{eff}^{100} from the average over the *clean* days to the average over the *mixed* days, this is as expected and as was concluded also above. When aerosols are present in the cloud layer, more aerosol will act as CCN, and therefore the cloud droplet number concentration increases. And, as the hypothesis was, the effective radius decreases.

In 2017 such a difference is not found. There is no increase in cloud droplet number concentration or decrease in effective radius perceived with this classification. The selections for the classification can be made finer or better and not all the days have to be included. When only the extreme cases for the three categories are taken into account, the effects could be studied in more detail.

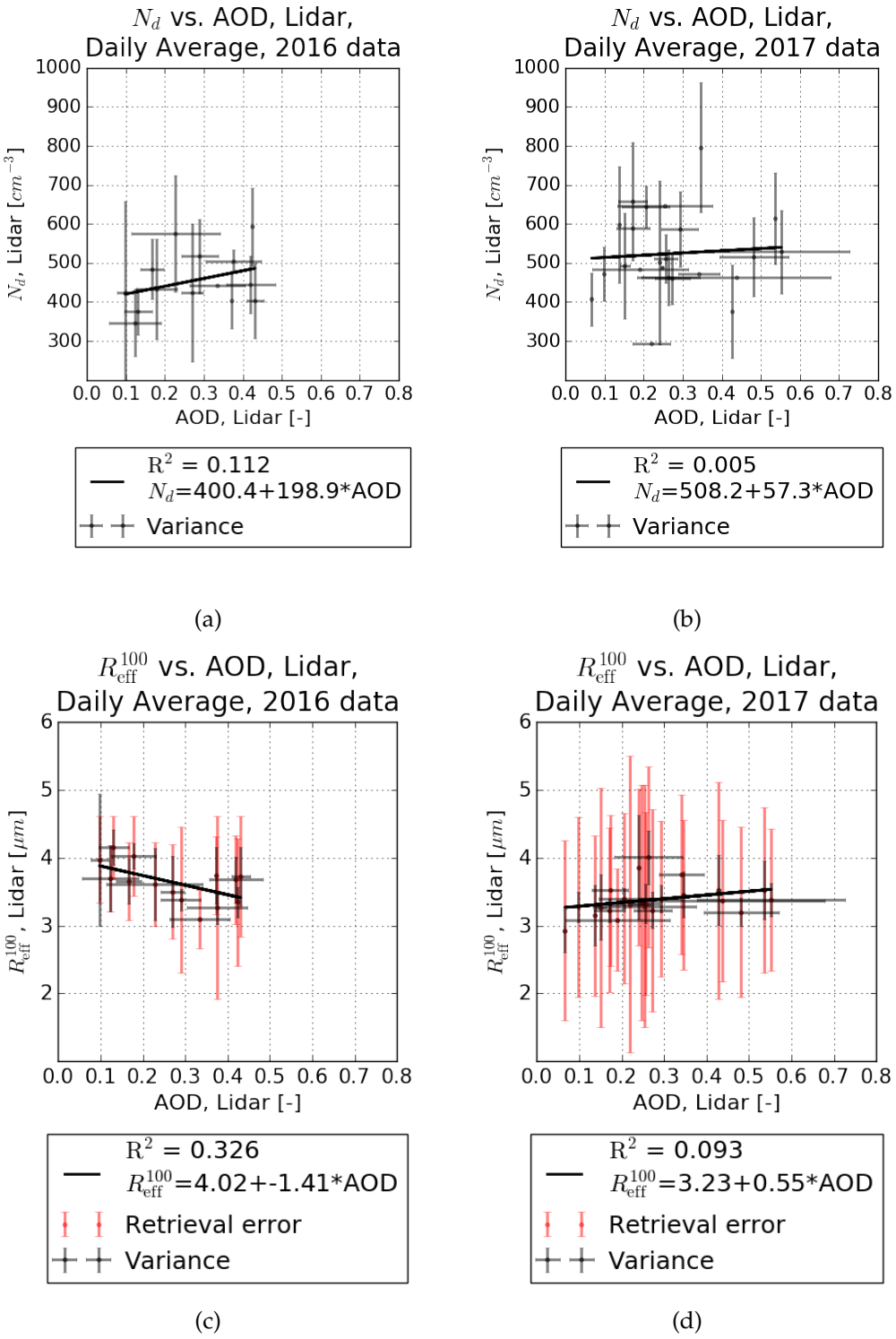

Figure 4.22: The daily averaged R_{eff}^{100}, N_d and AOD for the selections retrieved with the lidar in the 2016 and 2017 measurement period. The red error bars show the retrieval errors, 19.75 % and 39.05 % for the lidar R_{eff}^{100} retrieval in 2016 and 2017 respectively. For the number density and the AOD, the retrieval errors are significant smaller than the standard deviations from the averaging. So these retrieval errors are not shown in the figures. The gray error bars show the standard deviation in the day, the variation around the mean.

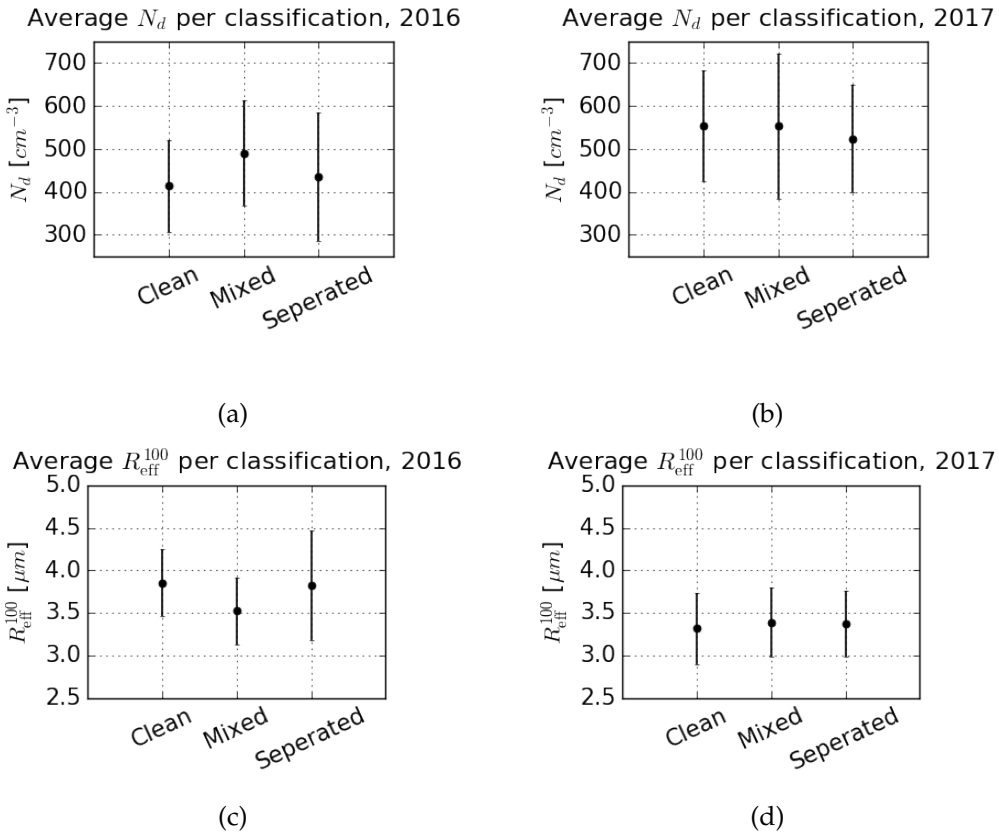

Figure 4.23: The R_{eff}^{100} and the N_d averaged per category. The categories are *clean*, *mixed* and *separated*, as explained in the text.

5. Discussion

AOD

The AOD results are retrieved from clear-sky selections made by a visual inspection using the raw data, the total lidar backscatter. The uncertainty from the predefined extinction-to-backscatter ratios S_{marine} and S_{dark} was calculated to be 8 % on average, 8.7 % in 2016 and 7.6 % in 2017, for the AOD when the predefined values for S_{marine} and S_{dark} were varied with 20 % from the standard value. The variation in z_0, and therefore a change in the value of the signal used in the boundary value problem assumed to be at the aerosol free altitude, has a bigger impact on the AOD results, a 7 % variation in the normalisation height, and thus the value of the signal used in the boundary value problem, results in a change in the average calculated AOD of 7 % on average, 2.3 % in 2016 and 8.9 % in 2017. The uncertainty due to z_0, and the value of the signal used in the boundary value problem, is larger in 2017 due to the low SNR.

The total retrieval error due to the estimation of the extinction-to-backscatter ratios and the normalisation height, and thus the signal used in the boundary value problem assumed to be at the aerosol free altitude, is 15 % on average over both years, 11 % in 2016 and 16.5 % in 2017. Random measurement errors arise from the noise in the aerosol extinction profiles, which is 9 % on average for the two measurement periods, 7.5 % in 2016 and 10.4 % in 2017. The total uncertainty for the AOD, retrieval plus measurement uncertainty, is 22.7 % on average for both measurement periods, 18.5 % in 2016 and 26.9 % in 2017. In 2017 this uncertainty is larger than in 2016 due to the low SNR caused by the misalignment. This uncertainty needs to be taken into account. To optimize the Klett inversion method, per selection a normalisation height could be estimated where the extinction is at its minimum, or the use of an altitude domain of 1 km at aerosol free altitude for the normalisation height can be further analyzed.

The AOD product for intercomparison is gathered from AERONET, the Calitoo and the Microtops. As the measurements by the different instruments are not done at the same moments, daily averages are compared. In 2016 a correlation between the AERONET data and our lidar retrievals exist. In 2017 this correlation is weak, this has to do with the low SNR and large uncertainties in 2017.

The vertical distribution of the aerosols can be studied with the lidar data by for example calculating the AODs for separated vertical layers. This can be used to study for example whether the aerosols are mostly in the boundary layer or in the free troposphere. The vertical distribution is dependent on the wind direction, wind speed, temperature vertical profile, humidity and the source of the aerosols.

HYSPLIT back-trajectories can be used to define the source of the aerosols as was shown. To study the vertical distribution of the aerosols, the characteristics of the aerosol and the dynamical processes should be studied further.

Cloud parameter

The main ARM site, where the measurements with the Cloud Radar were done, was situated 5 km to the east on Ascension Island, 300 m higher in altitude than our lidar. Because cloud characteristics can change significant over such a distance (Grabowski, 2000), this could make the intercomparison uncertain. And as was studied by Y. Blanchard, the cloud fraction above the main ARM site is not the same as the cloud fraction above the airport site, as we saw in figure 4.15. But because the main difference is in the low-level clouds, with a CBH below 1000 m, which are not included in the selections for the retrievals this difference in cloud characteristics is not of direct importance in our intercomparison, but should be taken into account in further analysis. The reference height used for the selections in the lidar method corresponds with the reference height used in the radar method. So the products at this reference height can be used for the intercomparison.

The retrieval of the cloud parameters with the MS based inversion method and the lidar data is done for both years, also after cloud selections have been made by a visual inspection using the raw data, the total lidar backscatter. The retrieval error in 2016 was 19.75 % and in 2017 39.05 %, due to the calibration, retrieval and measurement errors. In 2016 the lidar was just been serviced by Leosphere which made that the alignment was better than in 2017 and thus the SNR was higher in 2016 than in 2017.

The R_{eff}^{100} retrieved with Frisch's method 1 for the Radar data, used for the intercomparison are calculated with the variable daily averages calculated from the lidar retrieval as input for N_d. The uncertainties are calculated for Frisch's retrieval method 1, 5.7 % in 2016 and 5.6 % in 2017. Important is that drizzle cases are not included in the retrievals, as the reflectivity is highly sensitive to the size of the hydrometeors, and thus to drizzle. This gives an uncertainty from selecting drizzle-free periods for the selections for the retrieval.

The value for the lognormal spread of the cloud droplet size distribution used in the Radar retrieval is estimated on $\sigma_x = 0.34 \pm 0.09$. The sensitivity on the calculated R_{eff}^{100} due to the assumption on σ_x is analyzed. when σ_x is varied to 0.1 and 0.6, an average of 8.5 % change in R_{eff}^{100} is found. These are extreme values for σ_x, which would be unusual for a cloud droplet size distribution in marine stratocumulus clouds (Miles et al., 2000). So the values in between are potential values for σ_x, which results in a relatively small uncertainty in the R_{eff}^{100} retrieval.

In 2016 the Cloud Radar was only operating for 9 days of our measurement period, no intercomparison can be done. The intercomparison between our lidar retrievals and the radar retrievals for R_{eff}^{100} in 2017 correlate well. We see some

outliers in the radar method in the second week of the 2017 measurement period, this is caused by long periods of rain and therefore difficulties to make drizzle-free selections for the retrieval.

Frisch's method 2 is highly uncertain, the LWP measurements and the method itself have large uncertainties. The fact that the retrieved values for R_{eff}^{100} are on average a factor 3 larger than the retrieved values from Frisch's method 1, is not evaluated yet and therefore we only take into account the R_{eff}^{100} retrieval by Frisch's method 1 for the intercomparsion and further analysis.

Deriving Aerosol-Cloud interactions

In 2016 a clear relationship between the daily averaged R_{eff}^{100} and N_d with the daily averaged AOD is found. This was as expected, and gives evidence for the Twomey effect. This was also the conclusion from the analysis with the classification of the days for 2016. For 2017, these relationships were not found, because of the lower SNR and larger uncertainties in 2017.

The averaging over the days was necessary because measurements were not done at the same moments. But this averaging could have also been done over half days or quarter days, this can be done in further research. In the classification of the days all the days are included and assigned to a category. This can be improved, only the days that fit 100 % in a category could be included in the classification or parts of days can be used for the classification.

To be able to study the Twomey effect, one restriction on the situation is that the LWP should be constant. With the same amount of water available, increased aerosol will result in more droplets, and smaller R_{eff}, due to the increased competition of water by droplets. When water supply is sufficient, a positive relationship between the AOD and R_{eff} will appear owing to the collision-coalescence of droplets (Qiu et al., 2017). No LWP measurements were taken into account in the ACIs study yet. But the fact that the cloud selections in 2017 differed in the LWP (figure 4.21(b)) could also be an explanation for not finding the expected relationships between the R_{eff}^{100}, N_d and the AOD in 2017. The LWP data-sets should be included in further research to cope with the LWP constraint for the Twomey effect.

Qiu et al. (2017) also say that the dependence of R_{eff} on the aerosol is largest at heights near cloud base, therefore the reference height of 100 m for the cloud parameter R_{eff} will not be a limitation in studying ACIs.

Limitations in the ACI study next to the constraint on the LWP, are the relative small data sets, the spatial distance between measurements and the uncorrelated moments of measuring. Direct conclusions for the ACIs are highly uncertain. But an indication by using the daily averages for the AOD, R_{eff}^{100} and N_d and the categorization seems to provide evidence for the Twomey effect in 2016.

Validation of the retrievals

In the future, the alignment should be checked to increase the SNR. This would improve the results and decrease the uncertainty for the lidar retrieved AOD and cloud parameters.

To improve the validation method, measurements should be done at exactly the same moments in time at the same locations. Uncertainties will decrease a lot and direct intercomparisons case-by-case can be done. This could for example be done with a sun-photometer operating constantly situated next to the lidar to measure the AOD or with aircrafts, UAV's or drones to take in-situ measurements for the cloud parameters above the lidar.

The best opportunity for the validation of the lidar retrieval methods will be to compare them with airborne in-situ data. As the lidar operating on Ascension Island was part of the CLARIFY campaign, this was the plan beforehand. But because the in-situ aircraft data was not available yet during this research, and the ARM data was, the decision was made to start by comparing these products.

To further validate the AOD retrieval method and the cloud parameter retrieval method for the lidar data, the datasets from the CLARIFY campaign can be used. And other in-situ measurements can provide help full data to validate the methods. The spatial and temporal resolution will decrease, and uncertainties due to these effects will decrease. After validating the methods the data can be used to study the aerosol vertical profiles, the cloud parameters, the evolution of these and the interactions. HYSPLIT back-trajectories are necessary to study the sources of the aerosols, general meteorological data is useful to study the dynamical processes, to study the causes for the vertical distribution of the aerosols. Then the effect of this vertical distribution can be studied in relationship to the cloud parameters. The LWP constraint needs to be included in the end to study the ACIs.

6. Conclusions

In this research we compared the AOD and cloud parameter products retrieved from the UV-depolarisation lidar with the same products retrieved from other instruments and methods. We gathered a temporally dense dataset of lidar data over the two measurement periods. For the AOD we were able to compare our product in 2017 with AERONET, Calitoo and Microtops data, in 2016 only the AERONET data was available. For the cloud parameter intercomparison in both measurement periods, one similar retrieved product is used for the intercomparison, the cloud parameter R_{eff}^{100} calculated from radar reflectivity. We are now able to answer the three research questions, stated in the introduction.

The AOD retrievals from the lidar for the 2016 measurement period correspond well with the AOD values from AERONET. In 2017, the daily averaged lidar retrieved AODs correlate too little with the values from AERONET to draw conclusions. In 2017, the lidar was operating with larger retrieval errors because of a smaller SNR. Therefore the results in 2017 are overall less accurate.

For the cloud parameter intercomparison, not enough data points were available for 2016. In 2017, the R_{eff}^{100} retrieved from the lidar corresponds well within the uncertainty range with the radar retrieved R_{eff}^{100}. For Frisch's methods, the same as for the lidar MS based inversion method, assumptions are of big importance for the results, so the radar method is not naturally better than our lidar method, but because their results overlap within the uncertainty, confidence in our retrievals has increased.

The average calculated AOD retrieved from the lidar in 2016 and 2017 is similar, more fluctuation in the AOD seems to be present in 2017. Also the average R_{eff}^{100} over 2016 and 2017 is of similar value. For the aerosol and cloud conditions, when only taken into account the lidar results, the situation seems similar over the two measurement periods. Further analysis with meteorological conditions and taken into account the sources of the aerosol is required to prove the climatic comparability in the measurement periods.

At this moment of writing, the lidar is being realigned, the uncertainty in the calibration will decrease and a larger SNR would decrease the retrieval error. To decrease the uncertainty in the AOD retrieval, the Klett inversion method could be optimized, by defining a normalisation height per averaged selection, where the extinction is at its minimum or by using an altitude domain at aerosol free altitude. To further validate the cloud parameter retrieval from the lidar with high certainty, direct in-situ measurements at the same location as the lidar would be the best opportunity to verify the retrieval method. More data points corresponding in spatial location and temporally scale will improve the validation of our retrieved AOD and cloud products, and the ACI study. LWP data and binned data by the LWP value should be included in the ACIs analysis to study the Twomey effect.

The UV-depolarisation lidar and the retrieval methods described in this research can contribute to the ACI study and be used to improve climate models.

A. AOD retrieval

A.1. Lidar Calibration

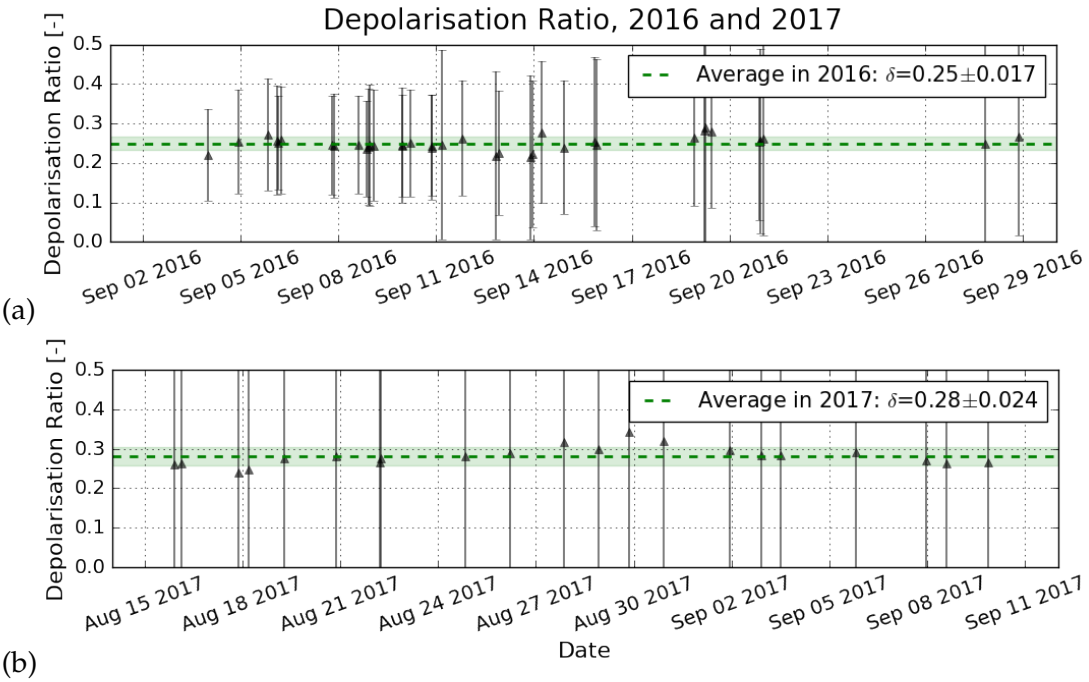

Figure A.1: The depolarisation ratio for clear sky selected height-time boxes for 2016 (a) and 2017 (b), without aerosols or clouds. To check the calibration of the lidar. With the gray error bar, the variation around the mean, the standard deviation, in the selected height-time box is shown. The total mean depolarisation ratio during the 2016 and 2017 measurement period separately is shown by the green dashed line, the shading around this line is the variation around this mean value, the standard deviation. The standard deviations for the selections is 0.18 on average for 2016 with outliers of 0.6, while in 2017 the average standard deviation is 0.54 with outliers up to 30.

A.2. Averaged AOD values from the uncertainty evaluation

Table A.1: Overview of the dependence on the calculated AOD from the predefined values for S and z_0. For the 2016 measurement period.

S_{marine}	$S_{aerosol}$	AOD, z_0=7000	AOD, z_0=6500	AOD, z_0=7500
20	40	0.236 ± 0.11		
20	50	0.247 ± 0.114		
20	60	0.257 ± 0.118		
25	40	0.25 ± 0.113		
25	**50**	$\mathbf{0.26 \pm 0.116}$	0.25 ± 0.117	0.262 ± 0.129
25	60	0.269 ± 0.119		
30	40	0.263 ± 0.115		
30	50	0.272 ± 0.118		
30	60	0.281 ± 0.121		

Table A.2: Overview of the dependence on the calculated AOD from the predefined values for S and z_0. For the 2017 measurement period.

S_{marine}	$S_{aerosol}$	AOD, z_0=7000	AOD, z_0=6500	AOD, z_0=7500
20	40	0.247 ± 0.126		
20	50	0.26 ± 0.13		
20	60	0.272 ± 0.133		
25	40	0.258 ± 0.128		
25	**50**	$\mathbf{0.27 \pm 0.132}$	0.287 ± 0.18	0.239 ± 0.19
25	60	0.281 ± 0.135		
30	40	0.267 ± 0.13		
30	50	0.278 ± 0.133		
30	60	0.288 ± 0.136		

A.3. Classification of days

Table A.3: The days of the 2016 measurement period divided in the categories *clean*, *mixed* or *separated*, as described in the text.

Clean	**Mixed**	**Separated**
03-09-2016	04-09-2016	10-09-2016
07-09-2016	05-09-2016	11-09-2016
08-09-2016	06-09-2016	14-09-2016
09-09-2016	12-09-2016	15-09-2016
17-09-2016	13-09-2016	16-09-2016
24-09-2016	18-09-2016	19-09-2016
29-09-2016	19-09-2016	27-09-2016
	20-09-2016	
	21-09-2016	
	22-09-2016	
	23-09-2016	
	28-09-2016	

Table A.4: The days of the 2017 measurement period divided in the categories *clean*, *mixed* or *separated*, as described in the text.

Clean	**Mixed**	**Separated**
15-08-2017	20-08-2017	18-08-2017
16-08-2017	21-08-2017	19-08-2017
17-08-2017	22-08-2017	26-08-2017
15-08-2017	24-08-2017	27-08-2017
23-08-2017	25-08-2017	30-08-2017
28-08-2017	29-08-2017	31-08-2017
	04-09-2017	01-09-2017
	05-09-2017	02-09-2017
	07-09-2017	03-09-2017
	08-09-2017	06-09-2017
		09-09-2017

B. Cloud parameters retrieval

B.1. Summary of the ECSIM MS based inversion method

MC approaches are always based on stochastic behaviour. In the ECSIM MC model the propagation of the laser photons is modeled in a stochastic manner. The photons are launched from the laser with an initial vector. The distance travelled by the photon before interacting with a scatterer or absorber is determined stochastically. The type and size of the particle that acts as scatterer or absorber is determined stochastically and if the photon is absorbed or scattered is then also determined stochastically according to the single-scatter albedo of the interacting particle. When the photon is scattered, the direction of the photon is changed according to its phase function.

The ECSIM MC model, unlike other MC models, is modified to increase computational efficiency. In usual MC models, photons are tracked until they are absorbed, detected or exit the simulation area. As any photon has a very small chance of being scattered back to the lidar receiver, the model is corrected for a certain amount of energy loss, by the absorption or the photon exiting the simulation area, in order to only evaluate the back scattered photons.

Table B.1: Range of parameters used in the MC calculations.

Parameter	**Values**
CBH [km]	0.5, 1.0, 2.0, 4.0
FOV [mrad]	0.5, 1.0, 2.0, 4.0
R_{eff}^{100} [µm]	2.0, 2.6, 3.3, 4.3, 5.6, 7.2, 9.3, 12.0
Γ_l [$\mathrm{g\,m^{-3}\,km^{-1}}$]	0.1, 0.2, 0.4, 0.6, 0.8, 1.0, 1.2, 1.4, 1.6, 1.8, 2.0

C. Abbreviations and Symbols

C.1. List of abbreviations

AOD	Aerosol Optical Depth
ACIs	Aerosol-Cloud Interactions
CCN	Cloud Condensation Nuclei
LWC	Liquid Water Content
LIDAR	LIght Detection And Ranging
AI	Aerosol Index
LWP	Liquid Water Path [$\mathrm{g\,m^{-2}}$]
AERONET	AErosol ROotic NETwork
ARM	Atmospheric Radiation Measurement Climate Research Facility
LASIC	Layered Atlantic Smoke Interactions with Clouds
CLARIFY	CLouds and Aerosol Radiative Impacts and Forcing
ORACLES	ObseRvations of Aerosols above CLouds and their intEractionS
AEROCLO-SA	AErosol RadiatiOn and CLOuds in Southern Africa
MWR	MicroWave Radiometer
MS	Multiple-Scattering
MC	Monte-Carlo
PMT	Photo-Multiplier Tubes
FOV	Field-Of-View
WSACR	W-band Scanning ARM Cloud Radar
KASACR	Ka-band Scanning ARM Cloud Radar
ATB	Attenuated Backscatter [$\mathrm{m^{-1}\,sr^{-1}}$]
SNR	Signal-to-Noise Ratio
Earth-CARE	Earth Clouds and Aerosol Radiation Explorer
ECSIM	Earth Clouds and Aerosol Radiation Explorer simulator
LUT	Look-Up Table
CBH	Cloud Base Height
BL	Boundary Layer

C.2. List of symbols

N_d	Cloud droplet number concentration [cm^{-3}]
R_{eff}	Cloud droplet effective radius [µm]
C_{lid}	Lidar calibration constant
δ^C	Polarisation cross-talk parameter
C_r	Inter-channel depolarisation calibration constant
C_N	Normalisation factor
P	Pressure [Pa]
T	Temperature [K]
τ	Aerosol Optical Depth
Z	Reflectivity factor [dB or $\mathrm{m}^6\,\mathrm{m}^{-3}$]
z	Range [m]
c	Speed of light [$\mathrm{m\,s}^{-1}$]
t	Time [s]
P	Lidar power
β	Backscatter coefficient [$\mathrm{m}^{-1}\,\mathrm{sr}^{-1}$]
α	Exctinction coefficient [m^{-1}]
S	Lidar ratio/Exctinction-to-backscatter ratio [sr]
ρ	Particle/Gas density [$\mathrm{kg\,m}^{-3}$]
λ	Wavelength [nm]
σ^R	Molecular Rayleigh backscattering cross section [$\mathrm{m}^2\,\mathrm{sr}^{-1}$]
M	Molecular mass [kg]
z_0	Normalisation height
Γ_l	Liquid water lapse rate
n	Cloud droplet distribution
R	Cloud droplet radius
σ_x	Logarithmic spread of the distribution

Bibliography

AEROCLO-SA (n.d.). *AErosol RadiatiOn and CLOuds in Southern Africa*. URL: http://www.hbao.cnrs.fr/.

AERONET (n.d.). *AErosol RObotic NETwork (AERONET)*. URL: https://gcmd.nasa.gov/KeywordSearch/Metadata.do?Portal=NASA&KeywordPath=Locations%7COCEAN%7CATLANTIC+OCEAN%7CSOUTH+ATLANTIC+OCEAN%7CASCENSION+ISLAND&OrigMetadataNode=GCMD&EntryId=AERONET_NASA&MetadataView=Full&MetadataType=0&lbnode=mdlb3.

ARM (n.d.). *Atmospheric Radiation Measurement Climate Research Facility (ARM)*. URL: https://www.arm.gov/.

(ARM), Instruments: KASACR (n.d.). *Atmospheric Radiation Measurement Climate Research Facility (ARM), Instruments: Ka-band Scanning ARM Cloud Radar (KASACR)*. URL: https://www.arm.gov/capabilities/instruments/kasacr.

(ARM), Instruments: MWR (n.d.). *Atmospheric Radiation Measurement Climate Research Facility (ARM), Instruments: Microwave Radiometer (MWR)*. URL: https://www.arm.gov/capabilities/instruments/mwr.

(ARM), Instruments: WSACR (n.d.). *Atmospheric Radiation Measurement Climate Research Facility (ARM), Instruments: W-band Scanning ARM Cloud Radar (WSACR)*. URL: https://www.arm.gov/capabilities/instruments/wsacr.

Blanchard, Yann (2018). 'Yann has found that cloud fraction is very different between the airport and the AMF site. It is unclear how different cloud microphysical and optical properties will be between these two sites.' In:

Brown, J. (2016). *Inverting ground-based polarisation lidar measurements to retrieve cloud microphysical properties during the Ascension Island Initiative*. Wageningen, Netherlands: URL: http://bibliotheek.knmi.nl/knmipubIR/IR2016-10.pdf.

Carlson, Toby N. and Joseph M. Prospero (1972). 'The Large-Scale Movement of Saharan Air Outbreaks over the Northern Equatorial Atlantic'. In: *Journal of Applied Meteorology* 11.2, pp. 283–297. DOI: 10.1175/1520-0450(1972)011<0283:TLSMOS>2.0.CO;2. eprint: https://doi.org/10.1175/1520-0450(1972)011<0283:TLSMOS>2.0.CO;2.

Cattrall, Christopher, John Reagan, Kurt Thome and Oleg Dubovik (2005). 'Variability of aerosol and spectral lidar and backscatter and extinction ratios of key aerosol types derived from selected Aerosol Robotic Network locations'. In: *Journal of Geophysical Research: Atmospheres* 110.D10. D10S11, n/a–n/a. DOI: 10.1029/2004JD005124.

CLARIFY (n.d.). *CLouds and Aerosol Radiative Impacts and Forcing (CLARIFY)*. URL: http://www.eufar.net/planning/xml_print.php?idp=clarify-2016_20150227151348.

Core Writing Team, R.K. Pachauri and L.A. Meyer (eds.) (2014). *IPCC, 2014: Climate Change 2014: Synthesis Report. Contribution of Working Groups I, II and III to the Fifth Assessment Report of the Intergovernmental Panel on Climate Change.* Geneva, Switzerland: IPCC.

Davidson, K. L., C. W. Fairall, P. Jones Boyle and G. E. Schacher (1984). 'Verification of an Atmospheric Mixed-Layer Model for a Coastal Region'. In: *Journal of Climate and Applied Meteorology* 23.4, pp. 617–636. DOI: 10.1175/1520-0450(1984)023<0617:VOAAML>2.0.CO;2. eprint: https://doi.org/10.1175/1520-0450(1984)023<0617:VOAAML>2.0.CO;2.

Donovan, D. P., H. Klein Baltink, J. S. Henzing, S. R. de Roode and A. P. Siebesma (2015). 'A depolarisation lidar-based method for the determination of liquid-cloud microphysical properties'. In: *Atmospheric Measurement Techniques* 8.1, pp. 237–266. DOI: 10.5194/amt-8-237-2015. URL: https://www.atmos-meas-tech.net/8/237/2015/.

Dorman, Clive E. and Robert H. Bourke (1981). 'Precipitation over the Atlantic Ocean, 30S to 70N'. In: *Monthly Weather Review* 109.3, pp. 554–563. DOI: 10.1175/1520-0493(1981)109<0554:POTAOT>2.0.CO;2. eprint: https://doi.org/10.1175/1520-0493(1981)109<0554:POTAOT>2.0.CO;2.

Eck, T. F., B. N. Holben, J. S. Reid, O. Dubovik, A. Smirnov, N. T. O'Neill, I. Slutsker and S. Kinne (1999). 'Wavelength dependence of the optical depth of biomass burning, urban, and desert dust aerosols'. In: *Journal of Geophysical Research: Atmospheres (1984–2012)* 104.D24, pp. 31333–31349. DOI: 10.1029/1999JD900923. URL: http:https://doi.org/10.1029/1999JD900923.

Fairall, C. W., J. E. Hare and J. B. Snider (1990). 'An Eight-Month Sample of Marine Stratocumulus Cloud Fraction, Albedo, and Integrated Liquid Water'. In: *Journal of Climate* 3.8, pp. 847–864. DOI: 10.1175/1520-0442(1990)003<0847:AEMSOM>2.0.CO;2. eprint: https://doi.org/10.1175/1520-0442(1990)003<0847:AEMSOM>2.0.CO;2.

Frisch, A. S., C. W. Fairall and J. B. Snider (1995). 'Measurement of Stratus Cloud and Drizzle Parameters in ASTEX with a K-Band Doppler Radar and a Microwave Radiometer'. In: *Journal of the Atmospheric Sciences* 52.16, pp. 2788–2799. DOI: 10.1175/1520-0469(1995)052<2788:MOSCAD>2.0.CO;2. eprint: https://doi.org/10.1175/1520-0469(1995)052<2788:MOSCAD>2.0.CO;2.

Frisch, A. S., Matthew Shupe, Irina Djalalova, Graham Feingold and Michael Poellot (2002). 'The Retrieval of Stratus Cloud Droplet Effective Radius with Cloud Radars'. In: *Journal of Atmospheric and Oceanic Technology* 19.6, pp. 835–842. DOI: 10.1175/1520-0426(2002)019<0835:TROSCD>2.0.CO;2. eprint: https://doi.org/10.1175/1520-0426(2002)019<0835:TROSCD>2.0.CO;2.

Grabowski, Wojciech W (2000). 'Cloud microphysics and the tropical climate: Cloud-resolving model perspective'. In: *Journal of Climate* 13.13, pp. 2306–2322.

Greatwood, Colin, Thomas S. Richardson, Jim Freer, Rick M. Thomas, A. Rob Mackenzie, Rebecca Brownlow, David Lowry, Rebecca E. Fisher and Euan G. Nisbet (2017). 'Atmospheric sampling on ascension island using multirotor UAVs'. In: *Sensors* 17.6, pp. 1–24. DOI: 10.3390/s17061189.

Guzzi, R. (2008). *Exploring the Atmosphere by Remote Sensing Techniques*. Lecture Notes in Physics. Springer Berlin Heidelberg, p. 231. URL: https://books.google.nl/books?id=RPRpCQAAQBAJ.

Holben, B.N., T.F. Eck, I. Slutsker, D. Tanré, J.P. Buis, A. Setzer, E. Vermote, J.A. Reagan, Y.J. Kaufman, T. Nakajima, F. Lavenu, I. Jankowiak and A. Smirnov (1998). 'AERONET—A Federated Instrument Network and Data Archive for Aerosol Characterization'. In: *Remote Sensing of Environment* 66.1, pp. 1–16. DOI: 10.1016/S0034-4257(98)00031-5. URL: http://www.sciencedirect.com/science/article/pii/S0034425798000315.

Ichoku, Charles, Robert Levy, Yoram J. Kaufman, Lorraine A. Remer, Rong-Rong Li, Vanderlei J. Martins, Brent N. Holben, Nader Abuhassan, Ilya Slutsker, Thomas F. Eck and Christophe Pietras (2002). 'Analysis of the performance characteristics of the five-channel Microtops II Sun photometer for measuring aerosol optical thickness and precipitable water vapor'. In: *Journal of Geophysical Research: Atmospheres* 107.D13, AAC 5-1–AAC 5-17. DOI: 10.1029/2001JD001302.

Illingworth, AJ, RJ Hogan, EJ O'connor, Dominique Bouniol, ME Brooks, Julien Delanoë, DP Donovan, JD Eastment, N Gaussiat, JWF Goddard et al. (2007). 'Cloudnet: Continuous evaluation of cloud profiles in seven operational models using ground-based observations'. In: *Bulletin of the American Meteorological Society* 88.6, pp. 883–898.

Kim, Jung-Hyun, Ralph R. Schneider, Stefan Mulitza and Peter J. Müller (2003). 'Reconstruction of SE trade-wind intensity based on sea-surface temperature gradients in the Southeast Atlantic over the last 25 kyr'. In: *Geophysical Research Letters* 30.22. 2144, n/a–n/a. DOI: 10.1029/2003GL017557.

Klett, James D. (1981). 'Stable analytical inversion solution for processing lidar returns'. In: *Appl. Opt.* 20.2, pp. 211–220. DOI: 10.1364/AO.20.000211. URL: http://ao.osa.org/abstract.cfm?URI=ao-20-2-211.

LASIC (n.d.). *Layered Atlantic Smoke Interactions with Clouds (LASIC)*. URL: https://www.arm.gov/research/campaigns/amf2016lasic.

Leosphere (n.d.). *EZ Lidar*. URL: https://tigerz.gsfc.nasa.gov/Documents/ezlidar.pdf.

Liou, Kuo-Nan and Richard M. Schotland (1971). 'Multiple Backscattering and Depolarization from Water Clouds for a Pulsed Lidar System'. In: *Journal of the Atmospheric Sciences* 28.5, pp. 772–784. DOI: 10.1175/1520-0469(1971)028<0772:MBADFW>

2.0.CO;2. eprint: https://doi.org/10.1175/1520-0469(1971)028<0772:MBADFW>2.0.CO;2.

Lohmann, U. and J. Feichter (2005). 'Global indirect aerosol effects: a review'. In: *Atmospheric Chemistry and Physics* 5.3, pp. 715–737. DOI: 10.5194/acp-5-715-2005. URL: https://www.atmos-chem-phys.net/5/715/2005/.

Mamouri, R.-E. and A. Ansmann (2016). 'Potential of polarization lidar to provide profiles of CCN- and INP-relevant aerosol parameters'. In: *Atmospheric Chemistry and Physics* 16.9, pp. 5905–5931. DOI: 10.5194/acp-16-5905-2016. URL: https://www.atmos-chem-phys.net/16/5905/2016/.

Martin, G. M., D. W. Johnson and A. Spice (1994). 'The Measurement and Parameterization of Effective Radius of Droplets in Warm Stratocumulus Clouds'. In: *Journal of the Atmospheric Sciences* 51.13, pp. 1823–1842. DOI: 10.1175/1520-0469(1994)051<1823:TMAPOE>2.0.CO;2. eprint: https://doi.org/10.1175/1520-0469(1994)051<1823:TMAPOE>2.0.CO;2.

McComiskey, A. and G. Feingold (2012). 'The scale problem in quantifying aerosol indirect effects'. In: *Atmospheric Chemistry and Physics* 12.2, pp. 1031–1049. DOI: 10.5194/acp-12-1031-2012. URL: https://www.atmos-chem-phys.net/12/1031/2012/.

McComiskey, Allison, Graham Feingold, A. Shelby Frisch, David D. Turner, Mark A. Miller, J. Christine Chiu, Qilong Min and John A. Ogren (2009). 'An assessment of aerosol-cloud interactions in marine stratus clouds based on surface remote sensing'. In: *Journal of Geophysical Research: Atmospheres* 114.D9. D09203, n/a–n/a. DOI: 10.1029/2008JD011006.

Measures, R.M. (1984). *Laser Remote Sensing: Fundamentals and Applications*. Wiley-Interscience publication. John Wiley & Sons. URL: https://books.google.nl/books?id=WflOAAAAMAAJ.

Miles, Natasha L., Johannes Verlinde and Eugene E. Clothiaux (2000). 'Cloud Droplet Size Distributions in Low-Level Stratiform Clouds'. In: *Journal of the Atmospheric Sciences* 57.2, pp. 295–311. DOI: 10.1175/1520-0469(2000)057<0295:CDSDIL>2.0.CO;2. eprint: https://doi.org/10.1175/1520-0469(2000)057<0295:CDSDIL>2.0.CO;2.

Müller, D., A. Ansmann, I. Mattis, M. Tesche, U. Wandinger, D. Althausen and G. Pisani (2007). 'Aerosol-type-dependent lidar ratios observed with Raman lidar'. In: *Journal of Geophysical Research: Atmospheres* 112.D16. D16202, n/a–n/a. DOI: 10.1029/2006JD008292.

Norris, Joel R. (1998). 'Low Cloud Type over the Ocean from Surface Observations. Part II: Geographical and Seasonal Variations'. In: *Journal of Climate* 11.3, pp. 383–403. DOI: 10.1175/1520-0442(1998)011<0383:LCTOTO>2.0.CO;2. eprint: https://doi.org/10.1175/1520-0442(1998)011<0383:LCTOTO>2.0.CO;2.

ORACLES (n.d.). *ORACLES Science Overview*. URL: https://espo.nasa.gov/oracles/content/ORACLES_Science_Overview_0.

Qiu, Yanmei, Chuanfeng Zhao, Jianping Guo and Jiming Li (2017). '8-Year ground-based observational analysis about the seasonal variation of the aerosol-cloud droplet effective radius relationship at SGP site'. In: *Atmospheric Environment* 164, pp. 139–146. DOI: 10.1016/j.atmosenv.2017.06.002. URL: http://www.sciencedirect.com/science/article/pii/S1352231017303746.

Rémillard, Jasmine, Pavlos Kollias, Edward Luke and Robert Wood (2012). 'Marine Boundary Layer Cloud Observations in the Azores'. In: *Journal of Climate* 25.21, pp. 7381–7398. DOI: 10.1175/JCLI-D-11-00610.1. eprint: https://doi.org/10.1175/JCLI-D-11-00610.1.

Rodgers, C.D. (2000). *Inverse Methods for Atmospheric Sounding: Theory and Practice*. Series on atmospheric, oceanic and planetary physics. World Scientific, p. 238. URL: https://books.google.nl/books?id=FjxqDQAAQBAJ.

Roode, Stephan R. de and Alexander Los (2008). 'The effect of temperature and humidity fluctuations on the liquid water path of non-precipitating closed-cell stratocumulus clouds'. In: *Quarterly Journal of the Royal Meteorological Society* 134.631, pp. 403–416. DOI: 10.1002/qj.222.

Sarna, K. and H. W. J. Russchenberg (2016). 'Ground-based remote sensing scheme for monitoring aerosol–cloud interactions'. In: *Atmospheric Measurement Techniques* 9.3, pp. 1039–1050. DOI: 10.5194/amt-9-1039-2016. URL: https://www.atmos-meas-tech.net/9/1039/2016/.

Sassen, Kenneth and Richard L. Petrilla (1986). 'Lidar depolarization from multiple scattering in marine stratus clouds'. In: *Appl. Opt.* 25.9, pp. 1450–1459. DOI: 10.1364/AO.25.001450. URL: http://ao.osa.org/abstract.cfm?URI=ao-25-9-1450.

scientists, The CLARIFY (2017). 'The CLARIFY team made a subdivision of the measurement period in 2017, regarding where the smoke was present, in the boundary layer, above, both or non.' In:

Stein, A. F., R. R. Draxler, G. D. Rolph, B. J. B. Stunder, M. D. Cohen and F. Ngan (2015). 'NOAA's HYSPLIT Atmospheric Transport and Dispersion Modeling System'. In: *Bulletin of the American Meteorological Society* 96.12, pp. 2059–2077. DOI: 10.1175/BAMS-D-14-00110.1. eprint: https://doi.org/10.1175/BAMS-D-14-00110.1.

Swap, R., M. Garstang, S. A. Macko, P. D. Tyson, W. Maenhaut, P. Artaxo, P. Kållberg and R. Talbot (1996). 'The long-range transport of southern African aerosols to the tropical South Atlantic'. In: *Journal of Geophysical Research: Atmospheres* 101.D19, pp. 23777–23791. DOI: 10.1029/95JD01049.

Szabó-Takács, Beáta (2011). 'Numerical simulation of the cycle of aerosol particles in stratocumulus clouds with a two-dimensional kinematic model'. In: 115, pp. 147–165.

Tenner, E.V. (2017). *The UV-LIDAR: A tool for investigating Aerosol-Cloud Interactions, a case study on Ascension Island*. Delft, Netherlands: URL: https://repository.tudelft.nl/islandora/object/uuid%3A2fa8eb2d-3523-4611-a006-7aa5f52e8ecd.

Tenum, Calitoo (n.d.). *Calitoo Aerosol photometer*. URL: http://www.calitoo.fr/uploads/documents/en/plaquette_eng.pdf.

Turner, D. D., A. M. Vogelmann, K. Johnson, M. Miller, R. T. Austin, J. C. Barnard, C. Flynn, C. Long, S. A. McFarlane, K. Cady-Pereira, S. A. Clough, J. C. Chiu, M. M. Khaiyer, J. Liljegren, B. Lin, P. Minnis, A. Marshak, S. Y. Matrosov, Q. Min, W. O'Hirok, Z. Wang and W. Wiscombe (2007). 'Thin Liquid Water Clouds: Their Importance and Our Challenge'. In: *Bulletin of the American Meteorological Society* 88.2, pp. 177–190. DOI: 10.1175/BAMS-88-2-177. eprint: https://doi.org/10.1175/BAMS-88-2-177.

Twomey, S. (1977). 'The Influence of Pollution on the Shortwave Albedo of Clouds'. In: *Journal of the Atmospheric Sciences* 34.7, pp. 1149–1152. DOI: 10.1175/1520-0469(1977)034<1149:TIOPOT>2.0.CO;2. eprint: https://doi.org/10.1175/1520-0469(1977)034<1149:TIOPOT>2.0.CO;2.

Wandinger, Ulla, Baars, Holger, Engelmann, Ronny, Hünerbein, Anja, Horn, Stefan, Kanitz, Thomas, Donovan, David, van Zadelhoff, Gerd-Jan, Daou, David, Fischer, Jürgen, von Bismarck, Jonas, Filipitsch, Florian, Docter, Nicole, Eisinger, Michael, Lajas, Dulce and Wehr, Tobias (2016). 'HETEAC: The Aerosol Classification Model for EarthCARE'. In: *EPJ Web of Conferences* 119, p. 01004. DOI: 10.1051/epjconf/201611901004.

Westwater, Ed R., Yong Han, Matthew D. Shupe and Sergey Y. Matrosov (2001). 'Analysis of integrated cloud liquid and precipitable water vapor retrievals from microwave radiometers during the Surface Heat Budget of the Arctic Ocean project'. In: *Journal of Geophysical Research: Atmospheres* 106.D23, pp. 32019–32030. DOI: 10.1029/2000JD000055.

Xu, Xiaofeng, Jinhuan Qiu, Xiangao Xia, Ling Sun and Min Min (2015). 'Characteristics of atmospheric aerosol optical depth variation in China during 1993-2012'. In: 119, pp. 82–94.

Zhang, S, H Xue and G Feingold (2011). 'Vertical profiles of droplet effective radius in shallow convective clouds'. In: *Atmospheric Chemistry and Physics* 11.10, pp. 4633–4644.

Zuluaga, Manuel D., Peter J. Webster and Carlos D. Hoyos (2012). 'Variability of aerosols in the tropical Atlantic Ocean relative to African Easterly Waves and their relationship with atmospheric and oceanic environments'. In: *Journal of Geophysical Research: Atmospheres* 117.D16. D16207, n/a–n/a. DOI: 10.1029/2011JD017181.